Title
NEUTRON ENERGY SPECTRA FROM NUCLEI EXCITED BY p--MESON CAPTURE

Author
Hagge, Donald E.

Publication Date
1963-06-12

UCRL-10516

University of California

Ernest O. Lawrence
Radiation Laboratory

NEUTRON ENERGY SPECTRA FROM NUCLEI EXCITED BY μ^-—MESON CAPTURE

Berkeley, California

DISCLAIMER

UCRL-10516
UC-34 Physics
TID-4500 (19th Ed.)

UNIVERSITY OF CALIFORNIA
Lawrence Radiation Laboratory
Berkeley, California

Contract No. W-7405-eng-48

NEUTRON ENERGY SPECTRA FROM NUCLEI EXCITED BY μ^--MESON CAPTURE

Donald E. Hagge
(Ph. D. Thesis)

June 12, 1963

Printed in USA. Price $2.00. Available from the
Office of Technical Services
U. S. Department of Commerce
Washington 25, D.C.

NEUTRON ENERGY SPECTRA FROM NUCLEI EXCITED BY μ^--MESON CAPTURE

Contents

Abstract v

I. Introduction 1

A. μ^--Mesic Atoms 3

B. μ^--Meson Nuclear Capture 4

II. Theory

A. Compound Nucleus 7

B. Direct Neutron Emission 10

1. Fermi Energy Distribution 12

2. Gaussian Energy Distribution 14

3. Percent Direct Emission 16

III. Experimental Method

A. General Description 20

B. Beam 22

C. Counter Telescope 25

D. Electronics

1. Beam Monitor and μ^--Meson Stopping 27

2. Neutron Detection and Identification System 27

3. Data Routing and Storage System 32

E. Data Collection 34

IV. Data Analysis

A. Pulse-Height-Analyzer Calibration and Proton-Spectrum Corrections 36

B. Neutron-Spectrum Derivation 40

C. Sources of Error

1. Statistical Counting and PHA Calibration Errors . . 42

2. Neutron Multiple Scattering in the Scintillator . . . 46

3. Neutron Absorption in Targets 46

V. Results and Discussion 47

Acknowledgments 71

Appendices

A. Neutron-Escape Probability 72

B. Nuclear Mean Free Path 75

C. Efficiency Function 76

References 79

NEUTRON ENERGY SPECTRA FROM NUCLEI EXCITED BY μ^--MESON CAPTURE

Donald E. Hagge

Lawrence Radiation Laboratory
University of California
Berkeley, California

June 12, 1963

ABSTRACT

The neutron energy spectra have been measured from nuclear capture of μ^- mesons in Al, Ca, Fe, Ag, I, Au, and Pb. Nuclear temperatures were deduced from the spectra according to the Weisskopf evaporation theory. Results were compared to other experimental measurements and consistency with compound nuclear theory was discussed. The direct neutron emission spectrum was calculated by using a degenerate Fermi gas model and momentum distributions of a Gaussian type.

The neutron detector was a liquid scintillation counter in conjunction with a pulse-shape discrimination circuit used for γ-ray rejection. The recoil-proton pulse-height spectra were unfolded by a computer code to obtain the neutron energy spectra. Measurements of neutrons from deuterium-tritium and PuBe sources indicate good reproduction of spectra if one simply assumes single collisions with hydrogen.

I. INTRODUCTION

When a μ^- meson is stopped in a target, it either decays from an atomic orbit or undergoes nuclear capture via an interaction of the form[1]

$$\mu^- + Z^A \rightarrow (Z - 1)^A + \nu. \tag{1}$$

Since the μ^- meson does not interact strongly, it penetrates the nucleus and interacts uniformly with the protons throughout the nuclear volume by means of the weak process

$$\mu^- + p \rightarrow n + \nu. \tag{2}$$

Approximately 100 MeV of energy is liberated in this reaction and, if the capturing proton is at rest, the resulting neutron has an energy of

$$E \approx \mu^2 c^4/2M_n c^2 = 6 \text{ MeV}.$$

However, since the nuclear protons have a momentum distribution, some of the neutrons may have much higher energy than this. In light nuclei, these neutrons have an appreciable chance of leaving the nucleus directly, and such neutrons comprise the direct-emission spectra. In intermediate and heavy nuclei, it is less probable that the neutrons will escape directly; rather, they will share their energy with the remaining nucleons to form a compound nucleus. The average excitation energy retained by the nucleus is between 15 and 20 MeV. This is indicated by the observation of about 1.5 neutrons emitted per μ^--meson capture by medium to heavy nuclei,[2] which also implies a more complex process than Eq. (2) alone. These neutrons from the compound nucleus comprise the evaporation spectra. There is emission of charged particles[3] also, but to a much lesser extent because of the nuclear Coulomb barrier. When the excitation energy remaining is insufficient to emit another bound nucleon, gamma radiation occurs until the ground state is reached.

The Bohr hypothesis states that the cross section for an (x, y) reaction can be written[4]

$$\sigma(x, y) = \sigma(x) P(y),$$

where $\sigma(x)$ is the cross section for the formation of a compound nucleus by capture of particle x, and $P(y)$ is the probability that the compound nucleus will decay by emission of particle y. The decay is independent of the method of formation. Therefore, one can study the nature of nuclear matter by exciting nuclei through various channels.

The decay of the compound nucleus has been observed after excitation by means of neutron,[5,6] proton,[7,8] and alpha-particle[9] scattering, and the results have been compared with the theory of the statistical model.[10] A further consistency check can be made on this description of nuclear matter by studying the excited nucleus formed by μ^--meson capture.

The nuclear capture of a μ^- meson is a method of exciting the nucleus to moderate excitation energies. Several experiments have measured the reaction products from this interaction.[11] By considering the elementary process [Eq. (2)] and by assuming a particular nuclear model it is possible to calculate the energies of the resulting neutrons and the subsequent nuclear excitations. One can then test the theory by predicting the neutron multiplicity distribution and average neutron emission for a given nucleus and comparing them with experimental measurements.

The degenerate Fermi gas model gives a nuclear excitation which is too low to predict the average neutron emission.[2, 12] Also, because of the implicit kinematic energy limit, it cannot explain why three or four neutrons are emitted in a certain fraction of the reactions. To increase nuclear excitations, Lang proposed using an effective mass smaller than M, the nucleon mass.[13] Kaplan et al. calculated neutron multiplicities by assuming both a degenerate and a non-degenerate Fermi gas and a reduced nucleon mass.[2] A different approach was made by Cole,[14] who used an alpha-particle model.

Neutron emission was calculated by Singer,[15] using the nuclear picture of the Brueckner theory. In this it is assumed that the nucleons move independently inside the nucleus and that internucleon correlations are accounted for by an effective mass and a momentum distribution that is obtained from the nuclear-matter wave function. None of the above models satisfactorily accounts simultaneously for the neutron multiplicity distributions and for average emission from various nuclei. Better agreement with experiment is obtained for average emission when nucleon clustering near the surface is taken into account.[16] Further requirements can be made of theoretical models by comparing predicted neutron energy spectra with experimental observations.

In this experiment, neutron energy spectra from μ^- capture in seven target nuclei were measured. The targets were chosen to agree with those used in earlier measurements of neutron multiplicity distribution and average neutron emission.[17] Nuclear temperatures were deduced from the energy spectra according to the simple evaporation theory.[18] Comparison was made with measurements from other modes of excitation. Values of the level-density parameter of compound-nuclear theory were calculated from the data and compared with shell-model predictions.[19,20]

Direct neutron-emission spectra were calculated. Two different momentum distributions for the nuclear protons and neutrons were assumed: a Fermi degenerate gas and a distribution deduced from Brueckner theory. The calculation of escape probability utilized optical potentials to obtain nuclear mean free paths, and accounted for surface phenomena by analogy to optical refraction and reflection.

A. μ^--Mesic Atoms

When a μ^- meson is brought to rest in a target, several processes occur sequentially.[21] Initially, the particle loses energy by ionization. When the μ^- is moving slowly enough, it is captured into an atomic orbit about the nucleus. With the concurrent emission of x rays,[22] it cascades into the K orbit in a time short compared with its decay time.[23] From the K orbit, the μ^- meson either decays or is captured

by the nucleus, the relative rate being determined by the nucleus to which it is bound.[1]

The decay rate of the bound μ^- meson is changed from that in the free state for three reasons.[24] First, the number of final states available is reduced through the decrease in available energy. Second, there is Doppler effect and time dilation due to the motion of the particle in its orbit. Third, the outgoing electron wave is distorted by the nuclear electric potential. The apparent lifetimes for μ^--meson decay have been measured in elements over a wide range in atomic number Z.[25] Experiments have been done to observe reaction products from the disappearing μ^- mesons.[11] Both observations are consistent with an interaction of the form of electron K capture,[26,27] Eq. (1) above.

The large mass of the μ^- meson in comparison with an electron results in the following: The orbital radius of the μ^- meson is smaller than that of an electron by the ratio of their masses, i.e., by a factor of about 207. Also, the μ^--meson binding energy is larger than that of an electron by the same factor. For radial quantum number n = 14, the μ^- meson is already inside the K orbit of the electron. For Z = 45, the nuclear radius is equal to the μ^--meson K-orbital radius. Consequently, the μ^--meson wave function overlaps the nuclear volume considerably for a large atomic number. This results in a high nuclear capture rate for the μ^- meson. It also reduces the atomic binding energy of the μ^- meson considerably from a pure Coulomb potential. The μ^--meson binding energies used in the calculations for this paper were obtained from a numerical solution of the Dirac equation including polarization correction[28] (see Table III).

B. μ^--Meson Nuclear Capture

The rate of nuclear capture of μ^- mesons from the K orbit has been calculated in the following way to be proportional to Z^4.[26] Assume a point nucleus and let $\psi(r)$ be the μ^--meson wave function, where r is its distance from the nucleus. The probability of finding

the μ^- meson at the nucleus is given by $|\psi(0)|^2$ Since each proton in the nucleus has equal probability of capturing the μ^- meson, the capture rate is then proportional to

$$\Lambda_{cap} \propto Z|\psi(0)|^2$$

The hydrogen wave function for the 1S state is

$$\psi(r) = 2(Z/a_\mu)^{3/2} \exp(-Zr/a_\mu) ,$$

where a_μ is the Bohr radius for the μ^- meson. Thus we have, for the capture probability,

$$\Lambda_{cap} \propto Z^4$$

For heavy nuclei in which the nucleus can no longer be considered a point and the μ^- meson wave function overlaps the nuclear volume, we have

$$\Lambda \propto Z_{eff}^4 ,$$

where Z_{eff} is the effective charge of the nucleus; Z_{eff} is less than the actual charge because the finite nuclear size no longer permits one to assume a point nucleus and, also, because the neutron excess in heavy elements reduces the number of final states available, as a result of the exclusion principle.[29]

Because of the above Z dependence, the nuclear-capture rate from K-atomic orbits is much larger than the decay rate of μ^- mesons in high-Z elements. The decay and capture rate for three elements are given in Table I as an example.

Table I. Decay and capture rates of μ^- mesons (from reference 24).

Element	Z	Lifetime (nsec)	Λ_d (10^5 sec^{-1})	Λ_c (10^5 sec^{-1})
Al	13	750	4.5	8.8
Fe	26	160	4.5	58.0
Pb	82	74	4.5	131.2

II. THEORY

A. Compound Nucleus

The statistical model of the compound nucleus is utilized in considering the decay of the nucleus. The evaporation theory of Weisskopf[18, 4] is outlined below. It is assumed that the excitation energy of the nucleus after the μ^--meson capture is high enough to excite many states, and that subsequent transitions proceed to many states of the residual nucleus. Further, it is assumed that thermal equilibrium is reached among all degrees of freedom in the excited nucleus, so that no memory of the exciting process is retained (as was stated earlier in the Bohr hypothesis).

Consider the disintegration

$$A \rightarrow B + x,$$

where A represents the compound nucleus with excitation energy U_0, B the residual nucleus with excitation energy U, and x the emitted particle of mass M and spin s with kinetic energy T. If Q_x is the binding energy of x in A, then

$$U_0 = U + Q_x + T. \tag{3}$$

Since the nuclear Hamiltonian is invariant under time reversal, one can apply the principle of reciprocity and obtain for P(T), the probability of emission of particle x with energy T per unit energy per unit time,

$$P(T)\,dT = \frac{(2s+1)}{\pi^2 h^3} M\sigma_{ba}\, T \frac{W(B, U)}{W(A, U_0)}\, dT, \tag{4}$$

where σ_{ba} is the cross section for the capture of particle x by nucleus B, and $W(A, U_0)$ and $W(B, U)$ are level densities of the nuclei. It is assumed that σ_{ba} does not vary with T.

In analogy with thermodynamics, one can express the level density in terms of entropy S

$$W(B, U) = \exp S(B, U). \tag{5}$$

Also, a nuclear temperature θ may be defined as

$$\frac{1}{\theta} = \frac{\partial S(B, U)}{\partial U} = \frac{\partial}{\partial U} \log W(B, U) = -\frac{\partial}{\partial T} \log [P(T)/T], \qquad (6)$$

where the last step follows from Eqs. (4), (5), and (6) above. By considering only the first term in a Taylor expansion of $\log [P(T)/T]$, one finds

$$W(B, U_0 - Q_x - T) = W(B, U_0 - Q_x) \exp(-T/\theta) .$$

Then, Eq. (4) above becomes

$$P(T)\,dT = \frac{2M\sigma_{ba}}{\pi^2 h^3} \frac{W(B, U_0 - Q)}{W(A, U_0)} T \exp(-T/\theta)\,dT,$$

after $s = 1/2$ has been inserted for a neutron. After normalizing to unit probability one obtains

$$P(T)\,dT = (T/\theta^2) \exp(-T/\theta)\,dT. \qquad (7)$$

For this spectrum, one can easily show the mean and median neutron kinetic energies to be

$$\overline{T} = 2\theta \quad \text{and} \quad T_m = 1.7\,\theta.$$

This spectrum is valid only over a small energy range because of the assumptions made in its derivation. The excitation energy U_0 of the compound nucleus must be not less than about 5 MeV to ensure that the level densities are high enough for statistical consideration. On the other hand, if the energy U_0 is greater than about 9 or 10 MeV, the observed spectrum will be a superposition of particles from different stages of a cascade process corresponding to different nuclear temperatures or residual energies. Le Couteur and Lang have considered the more general case of very high excitation energies by accounting for the cooling-down of the nucleus after emission.[30] By employing a computer code, one can generate a spectrum by tracing through the successive generations of an emission process

for any given initial excitation energy U_0.

The above spectrum is for a unique initial excitation energy U_0, which is related to a unique nuclear temperature θ through an expression for the level density. If, however, the nucleus is left with a distribution of excitation energies $f(U_0)$, the resultant energy distribution of the evaporated neutrons is given by[30]

$$N(T) = \int f(U_0)\, P(U_0, T)\, dU_0 \,. \tag{8}$$

The dependence of nuclear level density on excitation energy as derived from the free Fermi-gas model[10] is given by

$$W(U) = (K/U^2) \exp 2(aU)^{1/2} \,,$$

where K is a constant and "a" is the level-density parameter. This form is favored because it is simple and has reasonable theoretical motivation, and because it provides an approximate fit to experimental data.[10] By utilizing Eq. (6) above, one finds the relationship between nuclear temperature and residual nuclear excitation energy to be

$$\frac{1}{\theta} = \left(\frac{a}{U}\right)^{1/2} - \frac{2}{U} \,, \tag{9}$$

or alternatively,

$$a = \frac{U}{\theta^2} + \frac{4}{\theta} + \frac{4}{U}$$

The observed dependence of the parameter "a" on nuclear mass A has compared favorably with shell-model predictions.[19]

The expression

$$a = 0.0748\, (j_n + j_p + 1)\, A^{2/3} \tag{10}$$

is derived by Newton[20] and modified by Lang,[19] where j_n and j_p are effective values of angular momentum of the neutrons and protons near the Fermi level (tabulated in Ref. 20). Since j_n and j_p are roughly proportional to $A^{1/3}$, the dependence of "a" on A is approximately linear, as is observed experimentally.[10]

B. Direct Neutron Emission

The neutron-energy distributions inside nuclei resulting from μ^--meson capture are determined from the energy and momentum-conservation laws and from assumed energy distributions for the capturing protons.

The energy distributions of the neutrons that escape are then calculated in the following way: The nucleus is assumed to be a constant-density sphere. The probability that a neutron created at some point inside the nucleus will reach the surface without interaction is evaluated by using the mean free path in nuclear matter as determined by real and imaginary optical potentials (see Appendix B). The probability of the neutron's passing through the surface is then evaluated by the refraction and reflection effects as expressed by a critical angle of incidence and by a transmission coefficient, respectively. This picture is not valid in the low-energy region, where the neutron wavelength outside becomes very large. The source point is averaged over the nuclear volume, and the escape probability is then determined for a given energy neutron. The directly emitted neutron-energy distribution has the form

$$N(T) = P(E)\, F(E)\ , \tag{11}$$

where P(E) is the escape probability for a neutron of energy E inside the nucleus and F(E) is the internal-neutron energy distribution. The energy outside the nucleus is represented by T and is related to E by either a nuclear potential or by the neutron binding energy and the Fermi energy, depending upon the model. The escape probability P(E) is calculated in Appendix A.

The general conservation equations for a μ^- meson captured by the nucleus Z^A may be written as

$$\mu - B_\mu = \Delta M + k + Q,^* \tag{12}$$

---

*c = 1 in all equations.

and

$$\vec{k} + \vec{p}^{A}_{Z-1} = 0, \tag{13}$$

where $\vec{k}$ and $\vec{p}^{A}_{Z-1}$ are the momenta of the neutrino and the resultant nucleus, respectively; μ is the rest energy of the μ^- meson and B_μ its K-shell binding energy; Q represents both the excitation and kinetic energy of the $(Z-1)^A$ nucleus; and ΔM is the difference between the ground-state energies of the $(Z-1)^A$ and Z^A nuclei. It is convenient to write E_0 as the total energy available for excitation of the product nucleus and rewrite the energy conservation Eq. (12) as

$$\mu - B_\mu - \Delta M = E_0 = k + Q . \tag{12'}$$

If one assumes that the μ^- meson interacts with a single proton of momentum $\vec{p}$, transforming it into a neutron of momentum $\vec{q}$, one can write

$$\vec{k} + \vec{q} + \vec{p}^{A-1}_{Z-1} = 0,$$

where $\vec{p}^{A-1}_{Z-1}$ is the momentum of the "core" nucleus which is assumed not to participate in the interaction. Hence, one can also write

$$\vec{p} + \vec{p}^{A-1}_{Z-1} = 0,$$

and the momentum-conservation Eq. (13) becomes

$$\vec{p} - \vec{q} - \vec{k} = 0. \tag{13'}$$

The kinetic energy of the resultant nucleus is smaller than its excitation by a factor of $0(1/A)$, therefore Q is considered to be only the nuclear excitation, U_0.

The interaction probability for μ^--meson capture is proportional to the density of final states, $\left.\frac{dn}{dE}\right|_{E_0}$; thus, we have

$$\left.\frac{dn}{dE}\right|_{E_0} \propto \int d^3k d^3q d^3p f(\vec{p})\,(1 - g(\vec{q}))\,\delta(\vec{p} - \vec{q} - \vec{k})\,\delta(E_0 - k - U_0), \tag{14}$$

where the δ functions provide for the conservation of energy and momentum. The momentum-distribution density functions of the protons and neutrons are $f(\vec{p})$ and $g(\vec{q})$, respectively. These functions restrict the integral to occupied proton states and unoccupied neutron states only.

1. Fermi Energy Distribution

One can relate the nuclear excitation energy U_0 to nucleon momenta by assuming that in the Fermi gas a proton of momentum p is transformed into a neutron of momentum q, where the momenta are measured from the bottoms of their respective Fermi wells. The nuclear excitation, which is the energy gained by the nucleon in being converted from a proton to a neutron, may then be expressed by

$$U_0 = (q^2 - p^2)/2M - (q_0^2 - p_0^2)/2M$$

$$= \Delta E' - \Delta E. \qquad (15)$$

The neutron and proton momenta on the surfaces of their Fermi spheres are q_0 and p_0, respectively, and the $\Delta E'$ and ΔE are defined only for later convenience. Substitution of Eqs. (15) and (13') into Eq. (12') gives

$$E_0 = k - \Delta E - (k^2 + 2\vec{q} \cdot \vec{k})/2M \qquad (12'')$$

For a Fermi gas, $f(\vec{p})$ and $g(\vec{q})$ have the forms

$$f(\vec{p}) = \left[1 + \exp\left(\frac{p^2 - p_0^2}{2M\theta}\right)\right]^{-1}$$

and

$$g(\vec{q}) = \left[1 + \exp\left(\frac{q^2 - q_0^2}{2M\theta}\right)\right]^{-1}$$

where θ is the Fermi temperature (in MeV).

Substitution of these expressions and Eq. (12'') into Eq. (14) and integration over all variables but q gives

$$\left.\frac{dn}{dE}\right|_{E_0} \propto \int q \left\{ \int_{k_1}^{k_2} \frac{k\,dk}{1 + \exp\left[(k + q^2/2M)/\theta + a\right]} \right\} \left(1 - \frac{1}{1 + \exp\left[(q^2 - q_0^2)/2M\theta\right]} \right) dq, \tag{16}$$

where $$a = -(E_0 + q_0^2/2M)/\theta ,$$

$$k_2 = (M - q) - \left[(M - q)^2 - 2M(E_0 + \Delta E) \right]^{1/2}, \tag{17}$$

and $$k_1 = (M + q) - \left[(M + q)^2 - 2M(E_0 + \Delta E) \right]^{1/2}, \tag{18}$$

and where $$q_0^2/2M = (9\pi/4)^{2/3} (\hbar^2/2Mr_0^2)(1 - Z/A)^{2/3}$$

and $$p_0^2/2M = (9\pi/4)^{2/3} (\hbar^2/2Mr_0^2)(Z/A)^{2/3}.$$

Then we obtain $$\Delta E = (9\pi/4)^{2/3} (\hbar^2/2Mr_0^2)[(1 - Z/A)^{2/3} - (Z/A)^{2/3}].$$

The inside integral of Eq. (16) is not expressible in closed form and therefore is evaluated numerically by a computer for each value of q. Equation (16) may be put in the form

$$\left.\frac{dn}{dE}\right|_{E_0} \propto \int F(E)\, dE, \tag{19}$$

where F(E) is the energy distribution inside the nucleus of the neutrons created by μ^- capture. By folding the escape probability P(E) into this, as expressed by Eq. (11), one obtains the neutron direct-emission energy distribution N(T). The neutron kinetic energies inside and outside the nucleus are related by

$$T = E - (q_0^2/2M) - B_n$$

In the calculation, we used a value of $r_0 = 1.4$ fermis, consistent with nuclear reactions,[15] and also $r_0 = 1.25$ fermis, which is more consistent with electron scattering results.[31] The differences between the direct-emission spectra for the two values of r_0 were only slight. The results for $r_0 = 1.25$ fermis are shown in Fig. 1. The μ^--meson binding energies, neutron binding energies, and nuclear-mass differences for the involved nuclei are listed in Table III.

2. Gaussian Energy Distribution

The neutron-energy distribution is now derived on the basis of the Brueckner picture of nuclear matter.[15] The momentum distributions take the form

$$f(\vec{p}) \propto \exp(-p^2/a^2)$$

and

$$g(\vec{q}) \propto \exp(-q^2/a^2) ,$$

where $a^2/2M$ is a constant ranging from 14 to 20 MeV. Here we have for the excitation energy

$$U_0 = \frac{(q^2 - p^2)}{2M} - \frac{(q_0^2 - p_0^2)}{2M}$$

Substitution of these expressions as before into Eq. (14) and integration over all variables but q gives

$$\left.\frac{dn}{dE}\right|_{E_0} \propto \int q \left\{\exp[-q^2/a^2 + (2M/a^2)E_0]\ [1 - \exp(-q^2/a^2)]\right.$$

$$\left.\times[(k_1 + a^2/2M)\exp(-k_1 2M/a^2) - (k_2 + a^2/2M)\exp(-k_2 2M/a^2)]\right\} dq, \tag{20}$$

where k_1 and k_2 are in Eqs. (17) and (18) with $\Delta E = 0$. Equation (20) may be put into the form

$$\left.\frac{dn}{dE}\right|_{E_0} \propto \int F(E)\, dE , \tag{19}$$

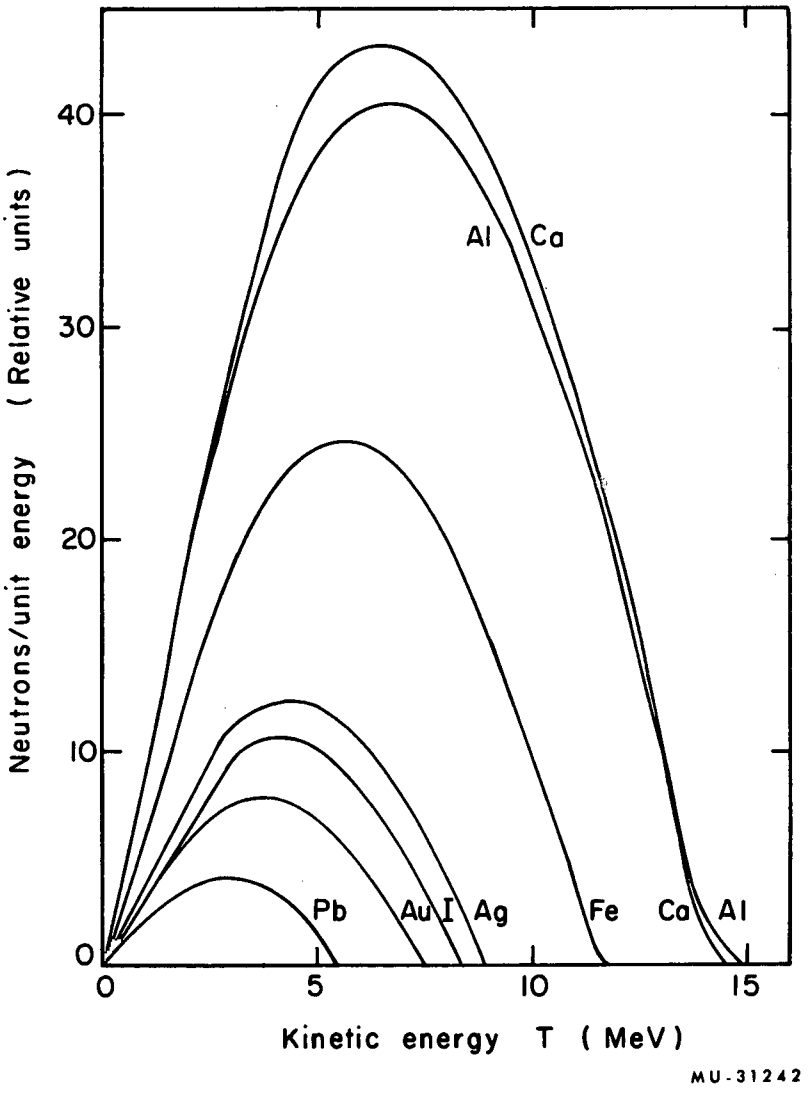

Fig. 1. Direct-emission neutron-energy spectra as calculated from Fermi degenerate gas model.

where F(E) is the energy distribution within the nucleus of the neutrons produced by μ^- capture.

The result of this calculation for calcium is shown in Fig. 2. The values $\alpha^2/2M$ = 14 MeV and M^* = 0.70 M were chosen.[15] Also shown for comparison in Fig. 2. are the results of our Fermi energy-distribution calculation (Sec. II. B. 1), a shell-model calculation by Dolinsky and Blokhintsev,[32] and a Fermi gas-model calculation by Lubkin.[33] It is observed that the peaking of the direct-emission spectrum from our Fermi gas model is only slightly higher in energy than that of the shell model and Lubkin's Fermi model calculation, while the Gaussian model has a much higher energy and broader peak. The Fermi gas-model calculations cannot predict the observed high-energy neutrons simply because of kinematical limitations. The Gaussian model would seem to predict an unreasonably high-energy direct-emission spectrum. Variations in the effective mass and α parameter about the chosen values had only a small effect on this feature.

3. Percent Direct Emission

The percentage of the observed neutrons that are directly emitted is calculated for the Fermi gas model, by utilizing measurements of observed average neutron emission.[17,34]

In the sketch, $G(T) = F[T + (q_0^2/2M) + B_n]$ is the energy distribution that would be observed if all those neutrons which have sufficient energy to escape the nucleus were to actually escape, and N(T) is the energy distribution of those neutrons which do escape in accordance with Eq. (11).

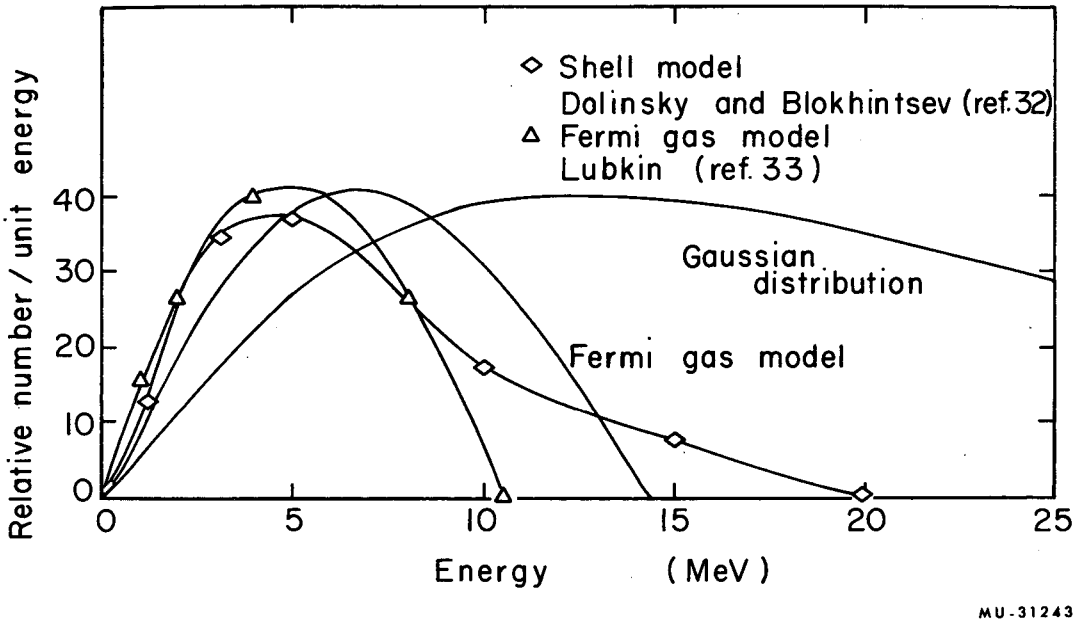

Fig. 2 . Direct-emission neutron-energy spectra for calcium.

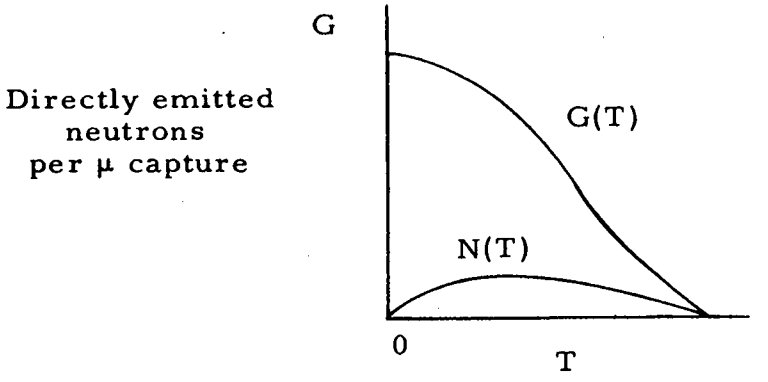

For each neutron that does not escape directly, (1 - N), there are on the average, $\bar{n}'$ neutrons evaporated [where N is the area under N(T)]. The observed average neutron emission is then given by

$$\bar{n} = \bar{n}' (1 - N) + N .$$

The fraction of the emitted neutrons that are direct (d. e.) is then

$$\text{fraction d. e.} = N/[\bar{n}' (1 - N) + N] = N/\bar{n} .$$

By measuring the areas under the curve N(T), as predicted by the Fermi gas model and escape-probability calculations, the results shown in Table II were found. For Ca an estimate of 7.4% was obtained, as compared with about 25% from the shell-model calculation by Dolinski and Blokhintsev and 2% from the spectrum predicted by Lubkin.

Table II. Percentage of neutrons directly emitted, as calculated from Fermi gas model.

Target nucleus	Average emission[a]	Direct emission (%)
Ca	0.73 ± 0.06	7.4
Fe	1.11 ± 0.05	3.9
Ag	1.52 ± 0.06	1.6
I	1.46 ± 0.06	2.0
Au	1.60 ± 0.06	1.3
Pb	1.64 ± 0.06	1.2

a. Reference 34

III. EXPERIMENTAL METHOD

A. General Description

The neutron-energy spectra from μ^--meson capture in the nuclei listed in Table III were measured. A negative beam of 220 MeV/c momentum from the Berkeley 184-inch cyclotron was used in the experiment. A scintillation-counter telescope determined the μ^- stoppings in the target. Electrons were rejected by a Cerenkov counter in anticoincidence with the telescope, and π^- mesons were eliminated by absorption in CH_2, by taking advantage of their having a shorter range than μ^- mesons of the same momentum. The neutron detector was a liquid scintillation counter. An anticoincidence scintillation counter, located between the target and the neutron detector, rejected charged particles. Gammas were distinguished from neutrons by a pulse-shape discriminator circuit which generated signals that were used to route the pulses from neutrons and gammas to different quadrants of a pulse-height analyzer (PHA). Background measurements were made simultaneously with data collection by the method indicated in Sec. III. D. 3. The PHA was calibrated by measuring the spectra from γ-ray sources of known energy. Measurements[37] of the liquid-scintillator response to electrons and protons were then used to relate the gamma ray and neutron energies.

Table III. Target nuclei and related data.

Natural Element	Z	A	Abundance (%)	ρ(g/cc)	B_n [b]	B_μ [c]	ΔM [b]	E_0
					(MeV)			
Al	13	27	100	2.70	6.437	0.46	3.13	102.03
Ca	20	40	100	1.55	7.798	1.05	1.83	102.74
Fe	26	56	100	7.86	7.270	1.72	4.22	99.68
Ag	47	107	51.35	10.50	6.390	4.76	0.81	100.09
		109	48.65		6.240	4.76	1.62	99.28
I	53	127	100	4.93	6.353	5.72	1.20	98.70
Au	79	197	100	19.32	5.540	10.22	1.26	94.19
Pb	82	204	1.37	11.35	6.620	10.66	1.28	93.72
		206	26.26		6.560	10.66	2.02	92.98
		207	20.82		6.800	10.66	1.95	93.05
		208	51.55		3.890	10.66	5.51	89.49

B_μ = μ^--meson K-orbit binding energy.

B_n = neutron binding energy in Z-1 nucleus.

$\Delta M = {}_AM^{Z-1} - {}_AM^Z$

$E_0 = \mu - B_\mu - \Delta M$

μ = 105.65 MeV

a: see Ref. 35.

b: see Ref. 36.

c: see Ref. 28.

B. Beam

The experimental layout is shown in Fig. 3.

The meson beam was produced by bombarding a 2-in. -thick Be target with 720-MeV protons in the 184-inch cyclotron. The negatively charged particles were momentum-analyzed by the cyclotron fringing field and brought out through the thin aluminum window of the vacuum tank. Then they passed through the internal quadrupole and the 8-ft-long iron collimator of the meson wheel. The beam was focused between the first external quadrupole and the bending magnet. After the 50 deg bend, the beam was refocused at the target position.

The two quadrupoles used, Sappho and Circe, are 8-in. doublets. The bending magnet used, Achilles, had 18 x 36-in. pole tips with an 8-in. gap.

The cave enclosing the counter telescope had 4-ft concrete walls and a 2-ft wooden roof.

While keeping the intensity as high as possible, the μ/π ratio was maximized in the following way. The particle flux through the telescope was maximized for a momentum of 200 MeV/c by moving the internal Be target both radially and azimuthally. Then the bending magnet current was increased by 10% to select the momentum of 220 MeV/c. This had the effect of shifting the apparent-source position. Since the μ source is diffuse and therefore larger than the π source, the loss in π intensity was greater than the loss in μ intensity. The net result was a larger μ/π ratio, although the absolute μ intensity was smaller.

The water Cerenkov counter was effectively 100% efficient in counting electrons in anticoincidence. Any remaining electron contamination had no adverse effect.

The π^- contamination was low, as can be seen from the range curve of Fig. 4. The prompt neutrons from π^- capture only served to increase the general background, without the possibility of being identified as μ^- capture neutrons; this was because of the gate circuitry which is explained in another section.

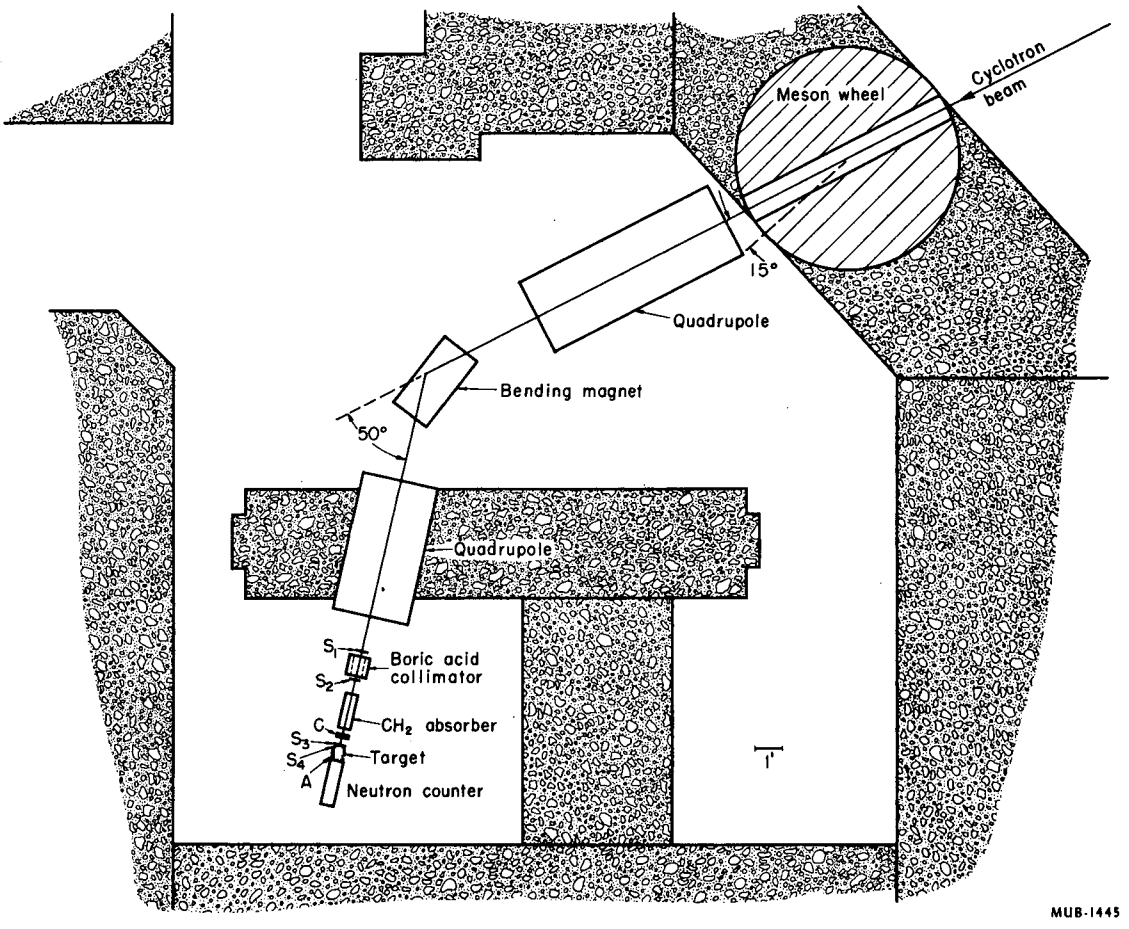

Fig. 3. Experimental layout in 184-inch cyclotron meson cave.

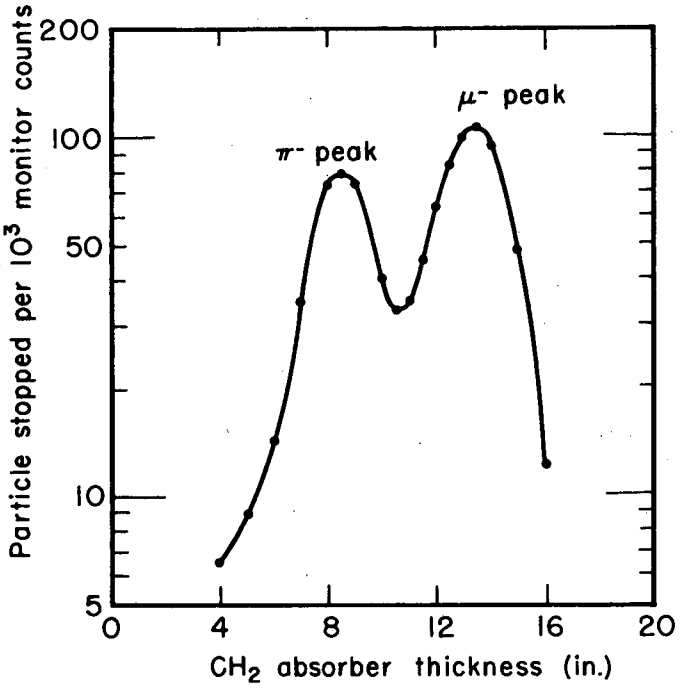

Fig. 4. Differential-range curve of 220-MeV/c meson beam.

The absorbing material used was CH_2 because neutron production from π^- stoppings is low and those neutrons produced are well moderated. The differential range curve is shown in Fig. 4. The experiment was run with 13-1/2-in. of CH_2 in place. The stopping rate in a 4 x 4-in. counter 1/4-in. thick for S_4 averaged about 10^5/min.

C. Counter Telescope

The counter telescope is shown in Fig. 5. All counters were made of 1/4-in.-thick plastic scintillator except counters C and N.

Counters S_1, S_2, and S_3 were 4 x 4-in. and were viewed by RCA 6655A photomultiplier tubes. Counters S_4 and A were 5-in. and 7-in. diam, respectively, and were viewed by RCA 6810A photomultiplier tubes. Counter C was a 5 x 5 x 1-in. water Cerenkov counter in a 0.125-in. lucite box and was viewed by an RCA 6810A photomultiplier tube. The neutron counter N contained Nuclear Enterprises 213 liquid scintillator (Nuclear Enterprises Ltd., Winnepeg, Canada). Most of the experiment was done with a 5-in.-diam x 1-in.-thick (inside dimensions) glass cell. This was sealed from the atmosphere to keep oxygen contamination low, a necessary condition for good pulse-shape discrimination. A 3/8-in.-thick cell also was used for a short time during the experiment as a check on neutron multiple scattering. The scintillator cell was viewed directly by an RCA 7046 photomultiplier tube.

Up to 16 in. of CH_2 absorber was available between counters S_2 and S_3. The amount of absorber could be adjusted from outside the cave to within 1/4 in. of any desired value.

Boric-acid bricks were used to provide collimation between counters S_1 and S_2 in order to help maintain a low accidental counting rate in the telescope.

The targets used in the experiment were placed between counters S_4 and A.

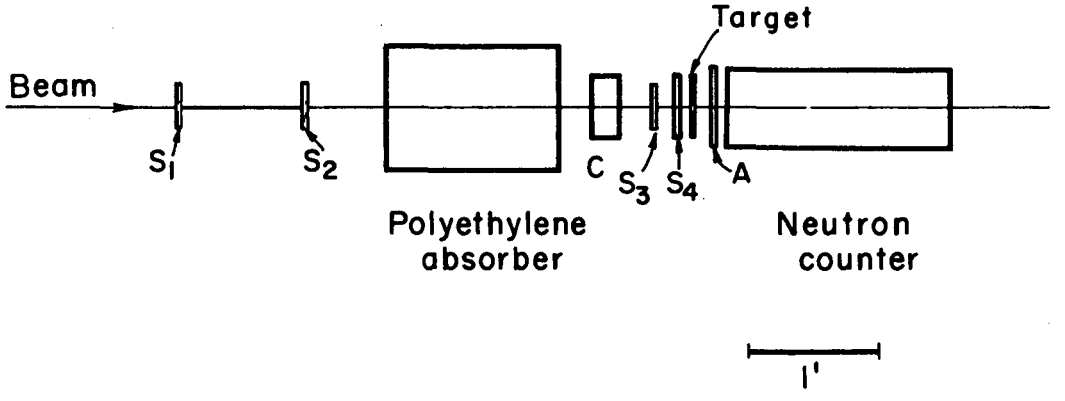

Fig. 5. Counter telescope.

D. Electronics

1. Beam Monitor and μ^--Meson Stopping Trigger

The electronics block diagram is shown in Fig. 6.

A beam monitor was provided by a double coincidence between counters S_1 and S_2. The counting rate was typically 10^6/min with full cyclotron beam.

A μ^--meson stopping trigger was provided by either coincidence circuit T_1 or T_2. The requirement for a trigger was pulses from counters S_2, S_3 and S_4, and no pulses from counters C and A within a time interval determined by the length of clipping lines in the coincidence circuits. This condition is denoted by $S_2S_3S_4\overline{CA}$ and indicates a μ^--meson stopping in the target.

Electrons of the proper momentum to enter the telescope gave Cerenkov light in counter C and were rejected. No π^--mesons of the proper momentum had sufficient range to pass through the absorber and count in S_3 and S_4.

The outputs of the above coincidence circuits were fed into 10 Mc transistorized discriminators and scaler units.

2. Neutron-Detection and Identification System

The detection and identification of neutrons in the presence of high γ radiation was accomplished through the use of Nuclear Enterprises organic liquid scintillator 213 in conjunction with pulse-shape discrimination circuitry.

The theory may be explained briefly as follows.[38, 39] A scintillation pulse is described as a combination of fast and slow components. In the scintillating material used here (as in certain others also) the relative amounts of these two components strongly depend upon the exciting particle. This is because the decay time of an ionized or excited molecule depends upon its environment and therefore upon the dE/dx loss of the particle in the medium. An ionized molecule recombines with an electron to form an excited molecule in a time related to the diffusion rate of electrons in the material. The light resulting from this mode of decay provides the

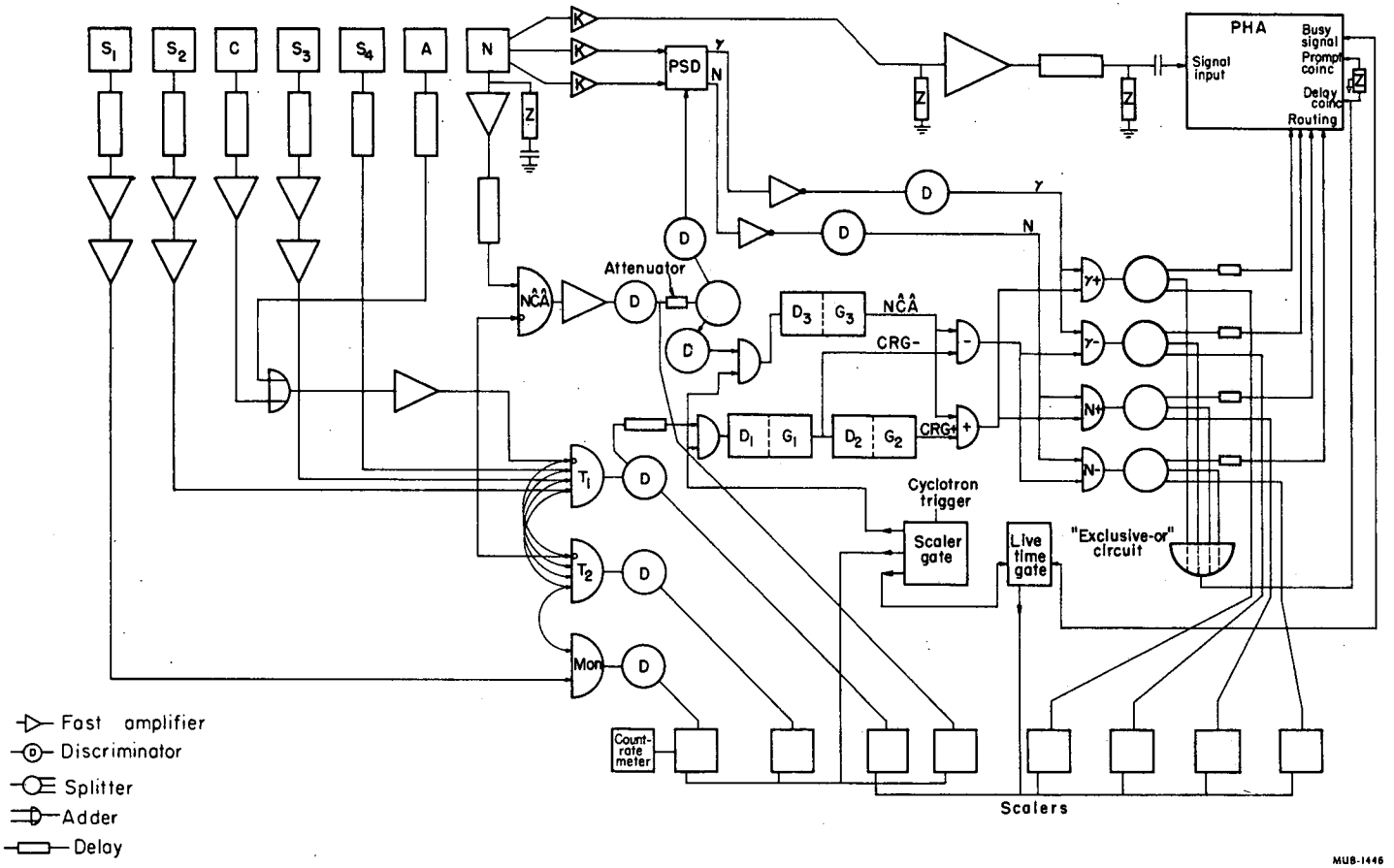

Fig. 6. Electronics block diagram.

slow component of the scintillation pulse:

$$\left.\begin{aligned} M^{+} + e^{-} &\rightarrow M^{*} + \text{photons} \\ M^{*} &\rightarrow M + \text{photons} \end{aligned}\right\} \quad \text{slow component}$$

An excited molecule decays by the emission of either photons or excitons. The light resulting from this mode of decay provides the fast component of the scintillation pulse:

$$\left.\begin{aligned} M^{*} &\rightarrow M + \text{photons} \\ M^{*} &\rightarrow M + \text{excitons} \end{aligned}\right\} \quad \text{fast component}$$

Neutrons produce recoil protons and γ rays produce Compton electrons in the scintillator. The ratios of the fast components to the slow components in the scintillation pulses from these two particles differ. This difference was detected by a circuit in the last dynode stage of the photomultiplier-tube base shown in Fig. 7. The capacitors of two identical RC circuits (time constant = 0.5 μsec) were charged, in different ways, by the last dynode-anode circuit, which is a low-impedance current source. One capacitor was charged through a Q6100 diode which presented a low impedance and short time-constant to the scintillation pulse. The other capacitor was charged through a 1-kΩ resistor which presented a higher impedance and longer time-constant to the pulse. The charge on the first capacitor provided a measure of the fast component of the light and its output is labeled "fast," whereas the charge on the second capacitor provided more of a measure of the total light and its output is labeled "slow." After having passed through cathode-follower amplifiers, these "slow" and "fast" signals entered the pulse-shape discriminator (PSD). A block diagram of this circuit is shown in Fig. 8.

The PSD attenuated the "fast" pulse and inverted and amplified the "slow" pulse to approximately the same amplitude. The sum of the two signals was either positive or negative depending upon the polarity of the input. A pulse from counter N with none from counter A

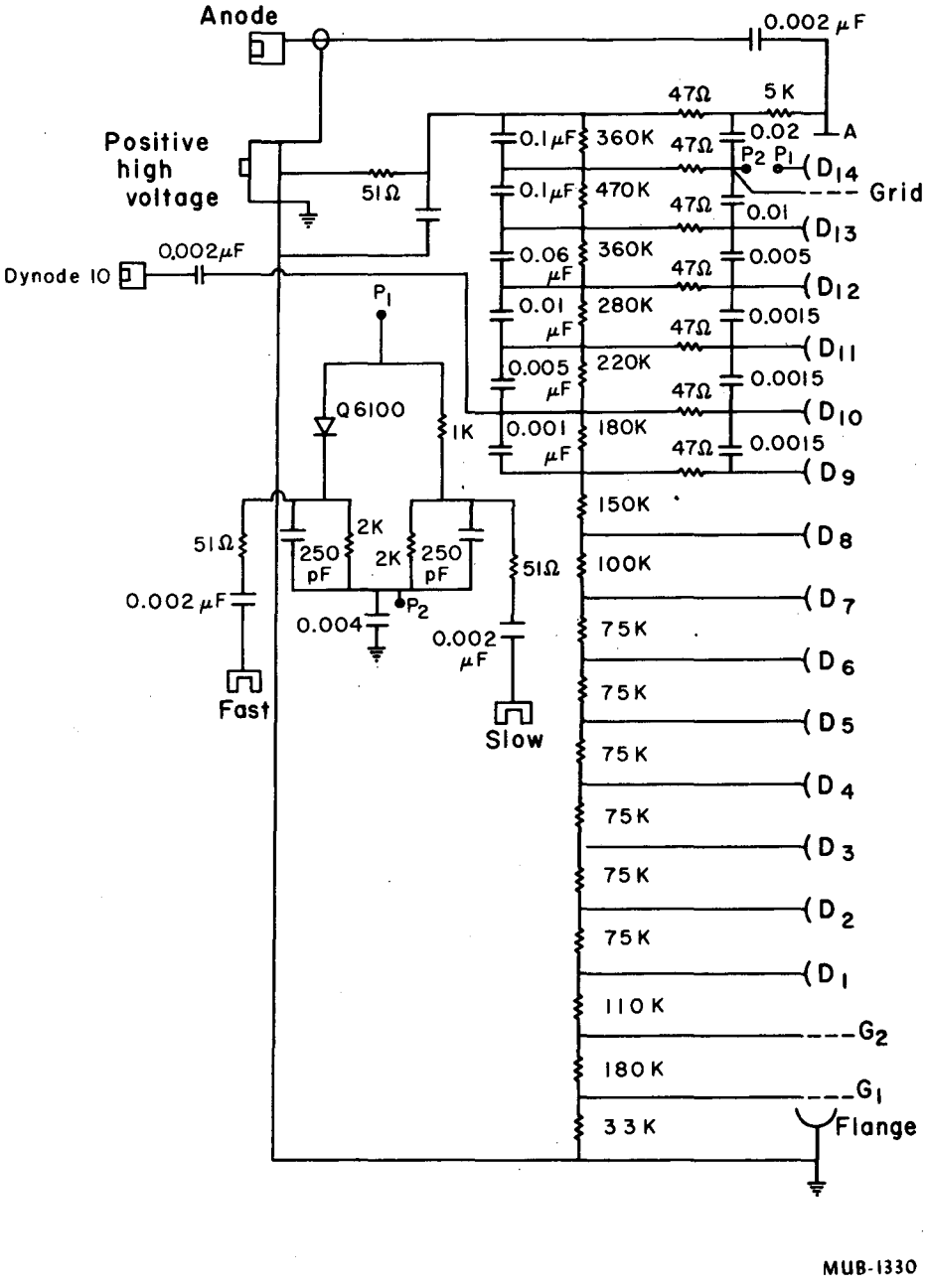

Fig. 7. Photomultiplier-tube base with pulse-shape discriminator circuitry.

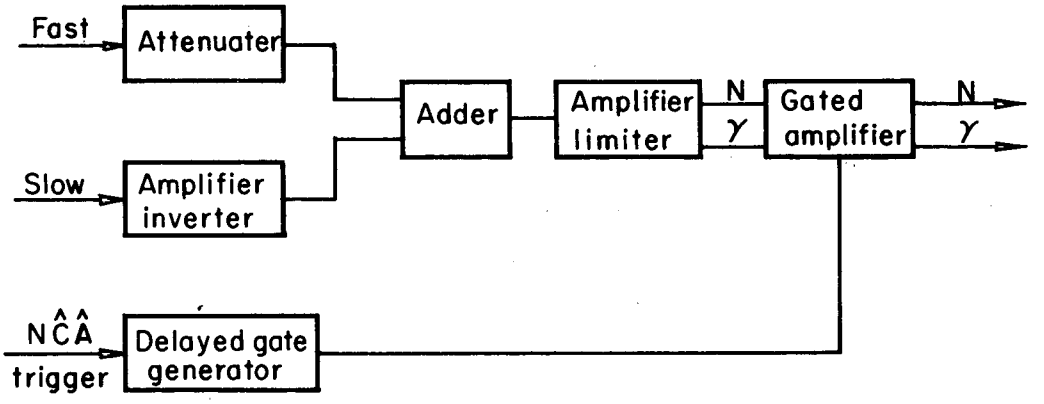

Fig. 8. Pulse-shape discriminator block diagram.

or C was required to generate a gate which allowed the N or γ signal to pass on to the routing circuits. This $N\overline{CA}$ requirement had the effect of reducing the PHA busy time. The $N\overline{CA}$ counts were scaled and recorded.

3. Data Routing and Storage System

A RIDL Model 34-12 400-channel pulse-height analyzer was used to measure and store the pulse-height distribution of the recoil protons and Compton electrons. The signal to be analyzed was taken from dynode No. 10 of the 7046 photomultiplier tube. This prevented saturation effects when the tube was operated at high voltages. The signal was amplified by a UCRL Model-6 transistorized linear amplifier before driving the PHA.

Both neutron and γ-ray spectra were stored in the PHA. Furthermore, neutron and γ-ray pulses were counted during equal intervals of time, both positive and negative in time with respect to a μ^--meson stopping trigger (refer to Fig. 9). A μ^- stopping triggered the delaying circuits and gate generators labeled D_1, G_1, D_2, and G_2 in Fig. 6. These gates are called the coincidence routing gates (CRG). An $N\overline{CA}$ pulse, which also gated the PSD, triggered the delaying circuit and gate generator labeled D_3 and G_3. Both the $N\overline{CA}$ pulse and μ^- stopping trigger were gated on during a selected portion of the cyclotron-beam spill by a scalar gate circuit. Gates G_1 and G_2 were set for equal time widths and located equidistant in time, negative and positive respectively, from prompt neutrons. Gate G_2, then, was open to counting particles for any desired length of time and at any time along the probability capture curve for a μ^--meson in a particular element. Typical gate settings are given in Fig. 9. The counts stored during G_1 represent a random background since they are detected before a μ^- stopping trigger and are not correlated with a μ^- capture event. The negative time spectrum was subtracted from the positive time spectrum.

A neutron or γ-ray pulse in coincidence with G_1 or G_2 gave either a negative time or a positive time routing pulse. These signals

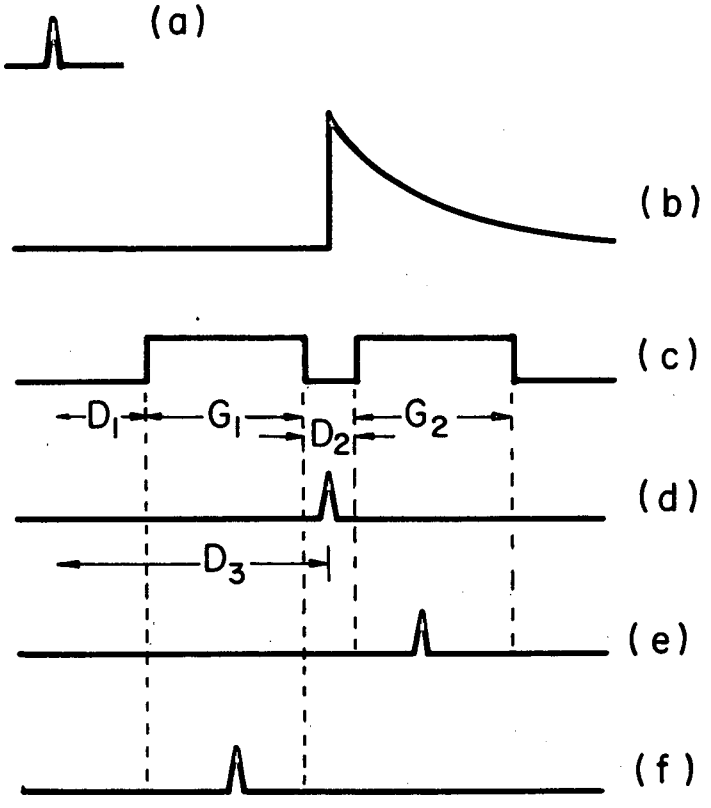

Fig. 9. Time relationship of gate particle pulses: (a) μ^--stopping trigger ($S_2S_3S_4\overline{CA}$); (b) μ^--capture probability curve (shown delayed from trigger pulse for illustrative purposes); (c) coincidence routing gates; (d) prompt neutrons; (e) μ^--capture neutrons; (f) background neutrons (the pulse on the last 3 traces is the output pulse from G_3 shown in Fig. 4.). Typical gate and delay times: $G_1 = G_2 = 300$ nsec, $D_1 = 750$ nsec, $D_2 = 50$ nsec.

were split, and along with the PSD N and γ signals, drove four coincidence circuits. The four possible outputs (N +, N -, γ +, γ -) were split three ways. They routed the N counter signal into one of the four 100-channel quadrants of the PHA. They drove a circuit that only gated the PHA on when there was a single input. They were scaled to provide the number of counts in each spectrum. During the time the PHA was busy storing information, a signal was fed back to prevent the scalers from counting.

E. Data Collection

Data runs were typically one hour in duration. The neutron counting rate varied between 200/min and 1000/min depending upon the target element, CRG settings, system gain, and beam intensity.

The data were read out of the PHA into a paper tape punch to minimize loss of running time. A paper tape reader and IBM typewriter were used to put the data into printed form.

The PHA was calibrated every few hours to maintain a check on gain stability. The calibration was done with the γ-ray sources listed in Table IV. The pulse-height spectrum for each source was measured and plotted. As an example, the Na^{24} spectrum is shown in Fig. 10. The energy calibration, using these spectra, is explained in the data-analysis section.

Table IV. γ-ray sources.

Source	γ-ray energy	Electron Compton edge energy
Cs^{137}	0.662	0.478
Na^{22}	1.276	1.063
Co^{60}	1.333	1.119
Na^{24}	1.368	1.153
Na^{24}	2.754	2.521

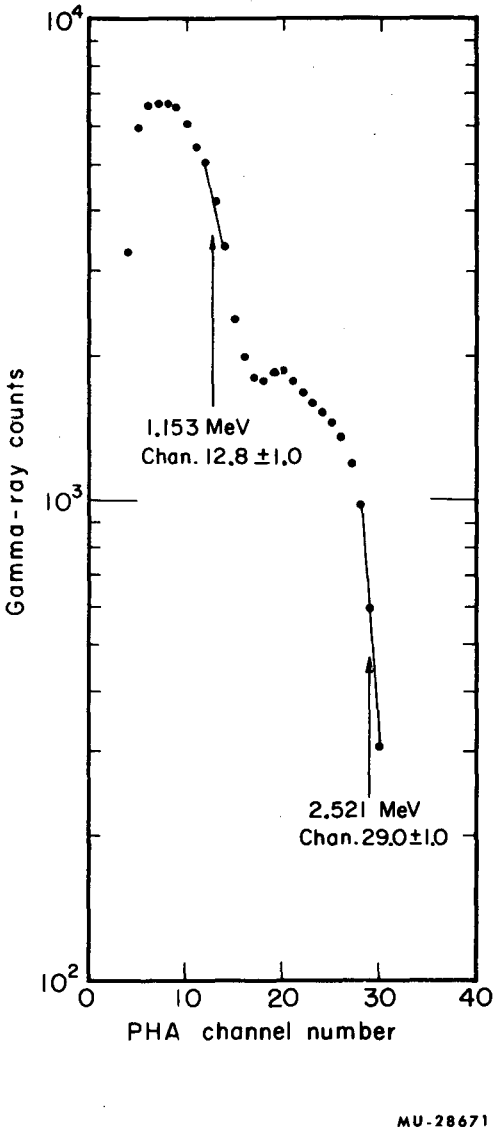

Fig. 10. PHA Na^{24} γ-ray spectrum.

IV. DATA ANALYSIS

A. Pulse-Height Analyzer Calibration and Proton-Spectrum Corrections

The PHA data were put into card form and handled completely by a code called "Neuspec," written for the IBM 7090 computer.

The pulse-height spectrum was in the form of proton counts per channel. A typical curve is shown in Fig. 11. The PHA was calibrated by measuring the pulse-height spectra of the γ-ray sources listed in Table IV. The Compton edges were determined and related to a PHA channel number as is shown for Na^{24} in Fig. 10. Since the PHA and the scintillator response to electrons are linear, one can determine a linear relation between electron energy and PHA channel number by using several sources. This is illustrated in Fig. 12. The Compton edge energies of the sources are listed in Table IV. The data point at channel 0 is determined from the PHA energy threshold. A least-squares-fit computer code was used to determine the intercept E_0, the slope, and the error matrices for each calibration run.

The light output of NE213 liquid scintillator from protons is not linear with energy in the region below about 5 MeV. Since it was desirable to have the pulse-height spectrum on a linear proton-energy scale, a correction was necessary. Measurements of the scintillator-light output for protons and electrons have been made.[37] An analytical expression, which relates the proton and electron energies for a given amount of light out, was determined from the data. This is shown in Fig. 13. The computer code, then, through the use of the above expression, determined the proton spectrum as desired.

The computer code divided the proton spectrum into bins of any chosen energy width. The position of the bins on the energy scale was movable in order to be able to utilize the lowest energy portion of the spectrum. When a channel was cut by bin limits, the code could divide the counts in two different ways. First, they could be divided in proportion to the energies on either side of the cut. The alternative

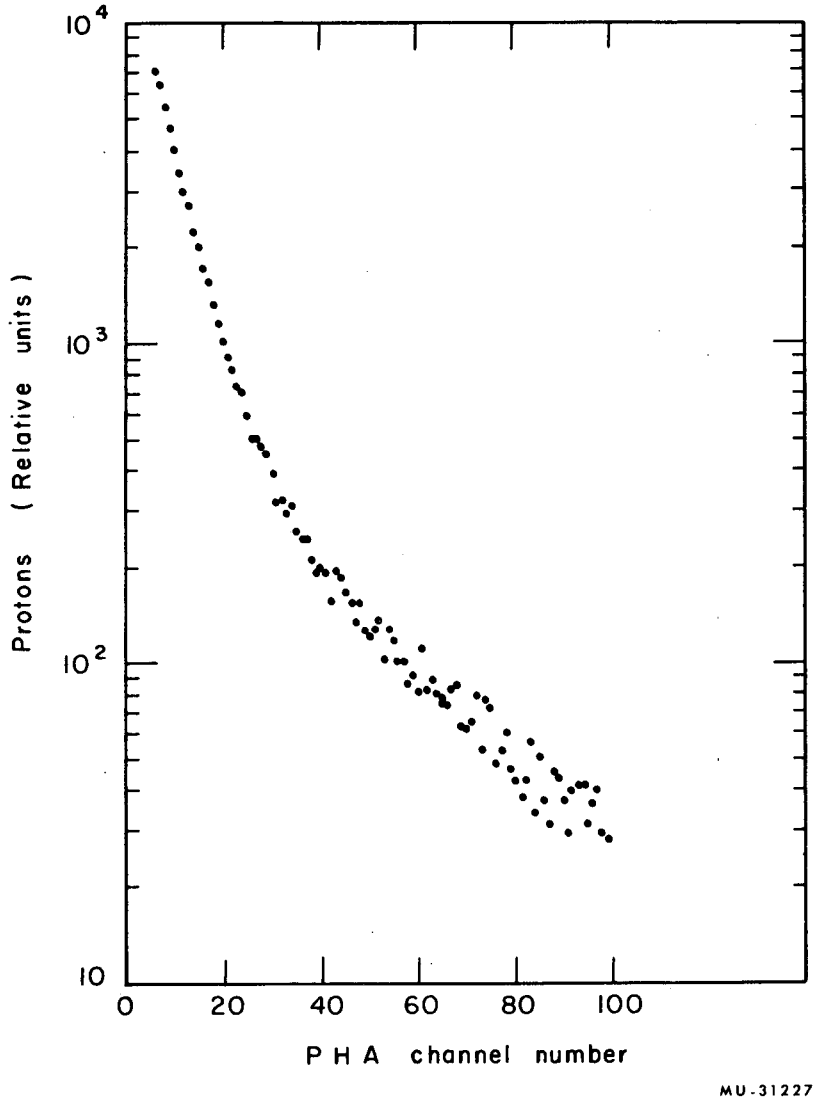

Fig. 11. Pulse-height analyzer proton spectrum.

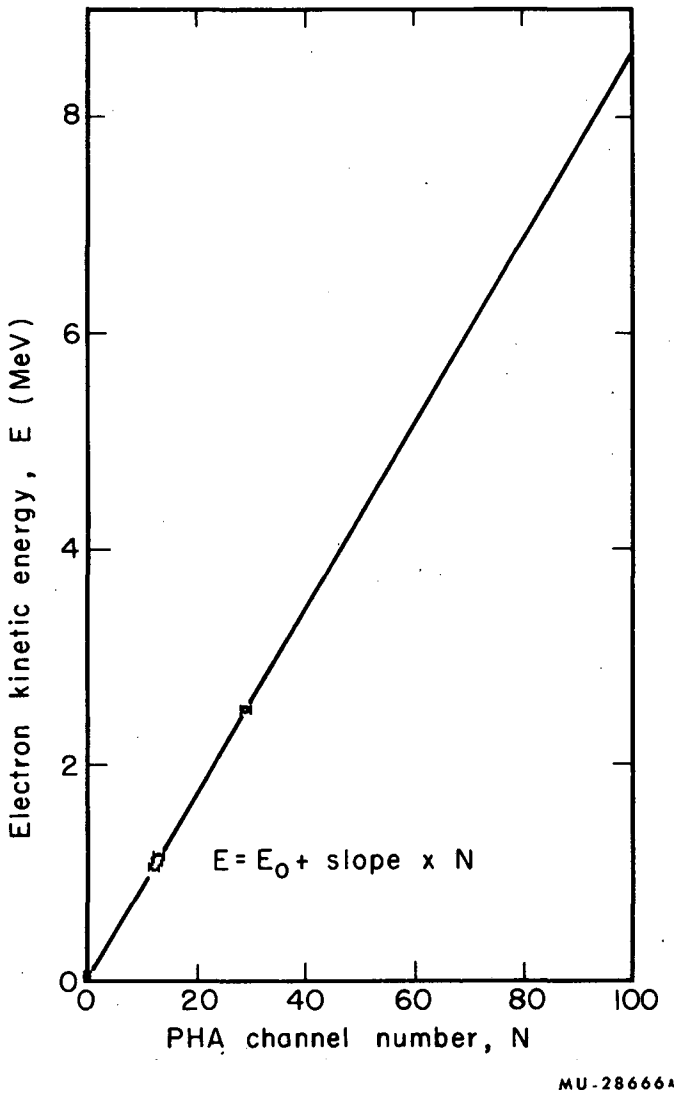

Fig. 12. PHA calibration from γ-ray sources.

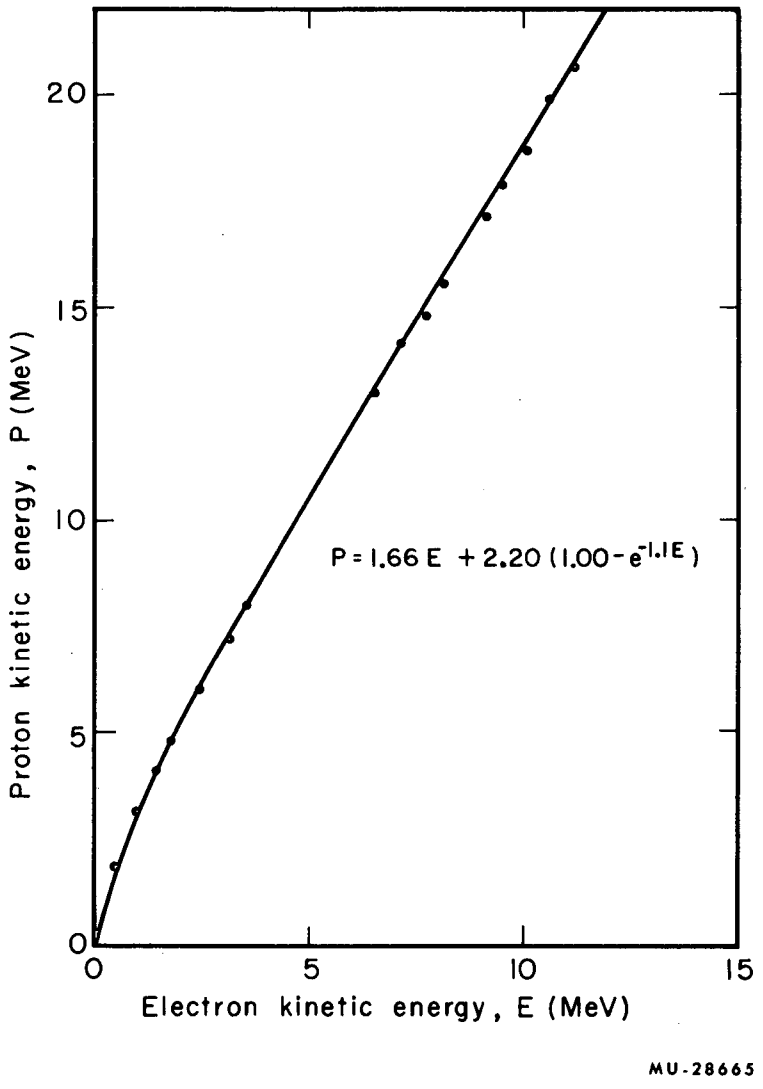

Fig. 13. Relative response of NE213 scintillator to protons and electrons. Data obtained from Batchelor et al. (ref. 37).

technique was to make a quadratic fit in energy with the adjacent channels and to divide the counts in proportion to the areas on either side of the cut. This method gave only slightly different results in the low-energy part of the spectrum where the slope was steep.

B. Neutron-Spectrum Derivation

Consider a mono-energetic beam of $N(E_0)$ neutrons making collisions at energy E_0. The scattered proton-energy distribution will be $dP(E)/dE$:

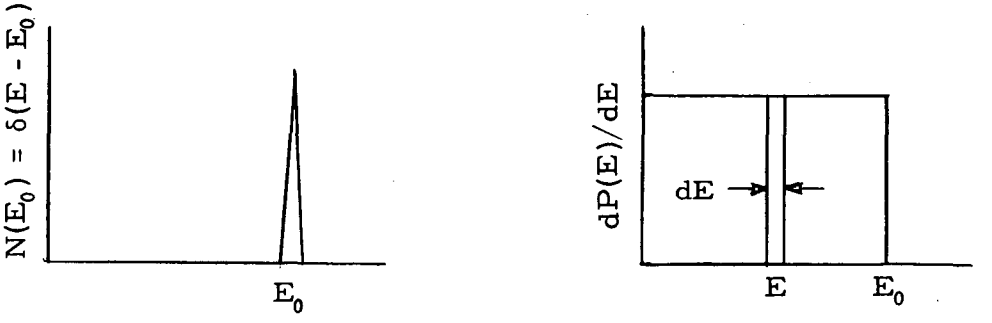

The number of protons in energy interval dE at E will be

$$dP(E) = \frac{dE}{E_0} N(E_0) .$$

For a distribution of neutrons N(E), since protons of energy E are produced by neutrons from E and above, this equation becomes

$$dP(E) = \int_E^\infty \left(\frac{dE}{E_0} N(E_0) \right) dE_0 .$$

Upon differentiation with respect to the lower limit one obtains

$$N(E) = -E\frac{d^2P(E)}{dE^2} = -E\frac{d}{dE}\left(\frac{dP(E)}{dE}\right) ,$$

where $dP(E)/dE$ is the corrected PHA spectrum. The n-p cross section varies with energy, therefore an efficiency function must be inserted to obtain the correct shape of the neutron-energy spectrum. The efficiency function is given by

$$F(E) = 1 - 1.074 \exp(-0.592/E^{1/2}).$$ (See Appendix C.)

The expression for the number of neutrons at energy E_i becomes

$$N_i = \frac{-E_i}{F(E_i)} \quad \frac{(P_{i+1} - P_i)}{(E_{i+1} - E_i)} ,$$

where N_i is the number of neutrons at energy E_i, and P_i is the number of protons in the ith bin that have energy E_i at the upper edge.

The proton spectra for each target were unfolded according to the above expression by the computer code. Each neutron spectrum was examined individually at the low-energy end for electronics threshold effect and for any systematic error. The proton spectra from all the runs for each element that possessed adequate statistics were then added together. Weighting factors for each spectrum were determined from the number of counts between specified energy limits of the calibrated proton spectra. The proton spectra for all targets were normalized to the same number of counts between identical energy limits. The statistical error on the points of a neutron spectrum is affected only by the number of counts in an unnormalized proton spectrum. The shape of the neutron spectrum is determined only by the slope of the proton spectrum. The position of the points of the neutron spectrum on the energy scale were adjusted so as to achieve the lowest possible energy point consistent with the thresholds of the individual runs. The end result was one neutron-energy spectrum for each target element.

A test on the analysis procedure and the energy resolution of

the system was provided by measuring the neutron-energy spectra of various sources.

The monochromatic 14.3-MeV neutrons from the deuterium-tritium reaction were measured. The spectrum is shown in Fig. 14. The location of the peak on the energy scale is excellent. The half width at half max is about ±10% at 15 MeV.

Frequent measurements were made of PuBe and mock fission sources. The energy spectra obtained are shown in Figs. 15 and 16 A comparison of our results is made with these two spectra as measured by emulsion experiments and with a calculation of the PuBe spectra.

The qualitative agreement of these data is the best available evidence that the over-all detection and analysis procedure correctly reproduces the neutron-energy spectra.

C. Sources of Error

1. Statistical Counting and PHA Calibration Errors.

The computer code "Neuspec" calculates and propagates the neutron statistical counting errors from the uncorrected PHA spectra.

A liberal uncertainty of ±1 channel was assigned to the PHA channel location of the γ-ray Compton edge (see Fig. 10). The least-squares-fit program, which determines the intercept and slope (see Fig. 12) for the PHA energy calibration, generates an error matrix[43] from these uncertainties in PHA channel numbers. This error matrix is necessary since the intercept and slope are correlated parameters of the fit. The computer code "Neuspec" then utilizes this error matrix and, along with the statistical error, determines the resulting total errors which appear on the neutron-energy spectra of Figs. 17 through 23.

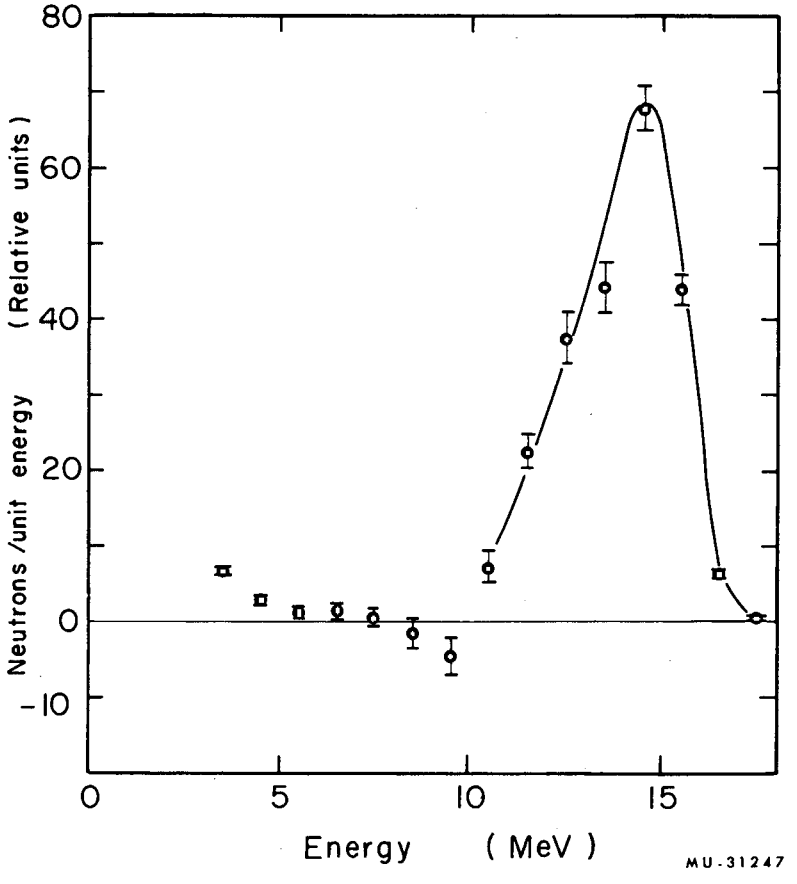

Fig. 14. 14-MeV neutron source.

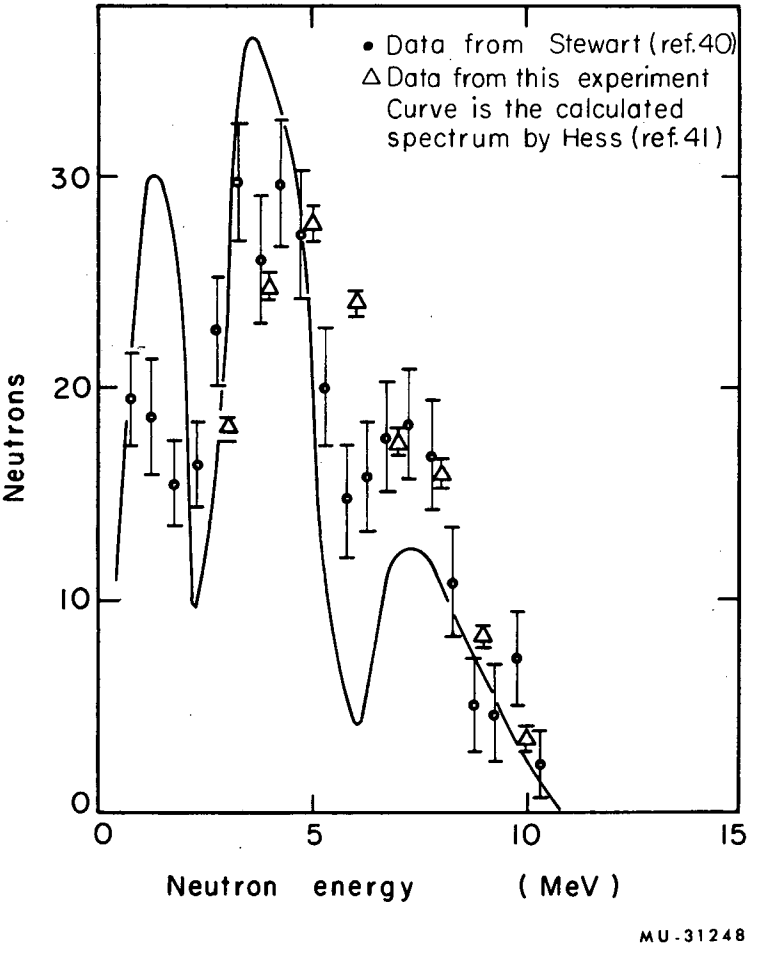

Fig. 15 PuBe neutron-energy spectrum.

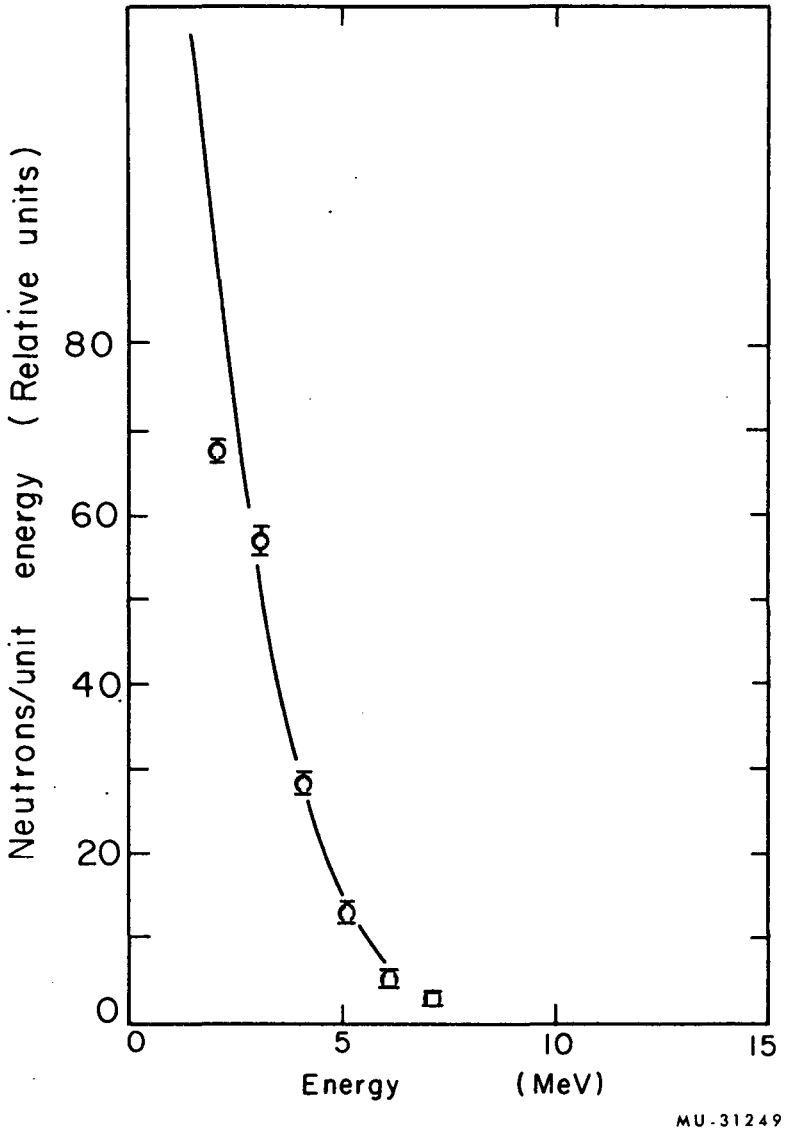

Fig. 16. Mock-fission spectrum. The curve is from the measurement by Watt (ref. 42).

2. Neutron Multiple Scattering in the Scintillator

A check was made on the validity of the single-collision assumption, which is used in the efficiency calculation in Appendix C. The spectrum of the 14.3-MeV neutrons from the deuterium-tritium reaction was measured. The 1-in.-thick liquid-scintillator capsule was oriented at 0, 60, and 90 deg, with respect to the neutron beam, to give 1, 2, and 5-in. path lengths, respectively, for the neutrons. The position and half widths of the spectrum did not change noticeably. The zero-deg spectrum is shown in Fig. 14.

A 3/8-in.-thick scintillator was used to measure the energy spectrum from lead to further check multiple scattering effects. Again, no change in the spectrum was perceptible.

3. Neutron Absorption in Targets

The neutron cross sections[46] for all target elements are slowly varying in the energy region of concern here. The absorption mean free paths are long compared to target thicknesses. Since we are concerned only with the shapes of the curves, no correction was made.

V. RESULTS AND DISCUSSION

The neutron-energy spectra from the seven targets used in the experiment are shown in Figs. 17 through 23. The same spectra, after the neutron counts are divided by their energy, are shown as semilog plots in Figs. 24 through 30. These will be referred to as nuclear temperature plots since, according to the simple evaporation theory as expressed by Eq. (7), the nuclear temperatures are simply the inverses of the slopes of the curves.

An increase of the low-energy part of the spectra relative to the high-energy tail, with increasing target atomic weight, is apparent. The parts of the spectra above 9 MeV appear to be constant and similar for all targets. Unfortunately, the response of the neutron-detection system did not extend to a low enough energy for an observation of the peaking of the evaporation spectra to be made.

If the nuclear excitation energy from μ^- capture were constant and low enough so that multiple neutron emission were negligible, any deviation from a straight line in a nuclear-temperature plot would be due to direct emission. This should provide a convenient test of direct-emission-spectra predictions since evaporation neutrons dominate the low-energy portion of observed spectra. A straight-line extrapolation to higher energies should therefore separate the spectra into direct and evaporation. However, since as many as four neutrons per capture are observed occasionally,[2] a deviation from a straight line is already inherent in the evaporation spectrum alone. The excitation energies are too high for the simple theory expressed by Eq. (7) to hold. Furthermore, the nuclear excitation energy is not unique; rather, it depends upon the kinematics of the μ^--meson proton interaction [Eq. (2)]. Therefore, the compound nucleus that is formed by μ^- capture cannot be described by a single nuclear temperature; instead, it is characterized by a distribution of temperature that is related to a distribution of excitation energies.[30] However, the concept of nuclear temperature is only specifically useful when it can be directly related

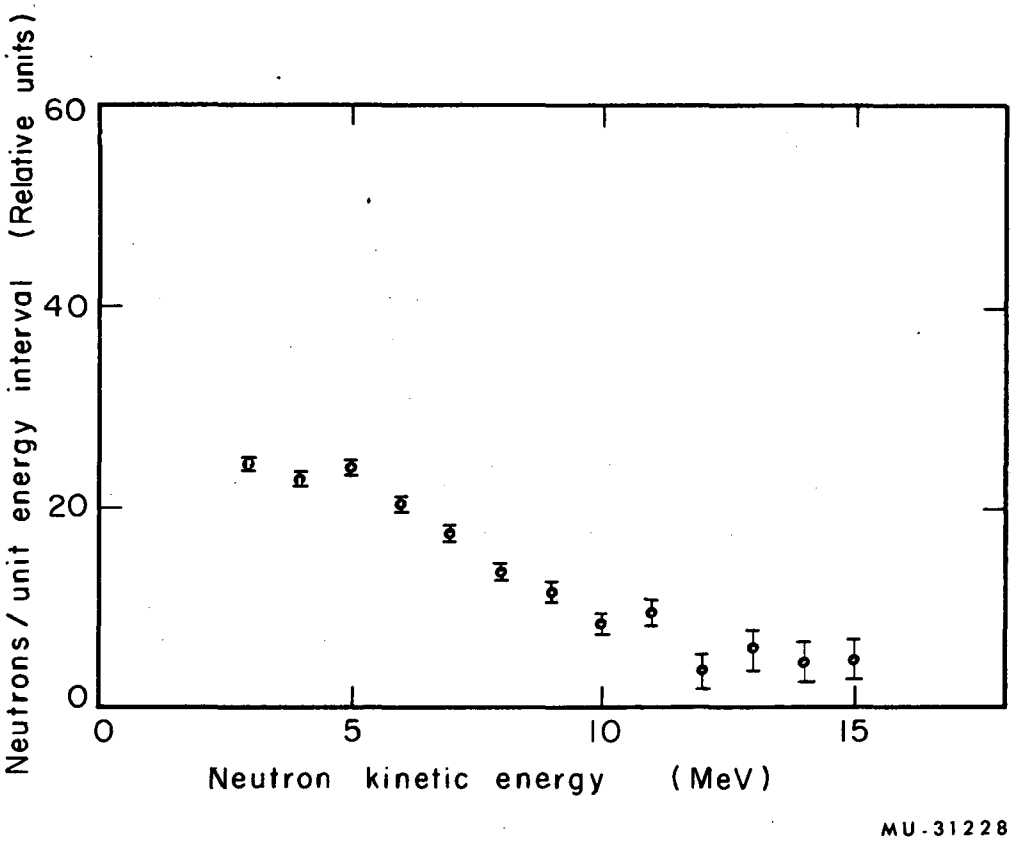

Fig. 17. Neutron-energy spectrum for aluminum.

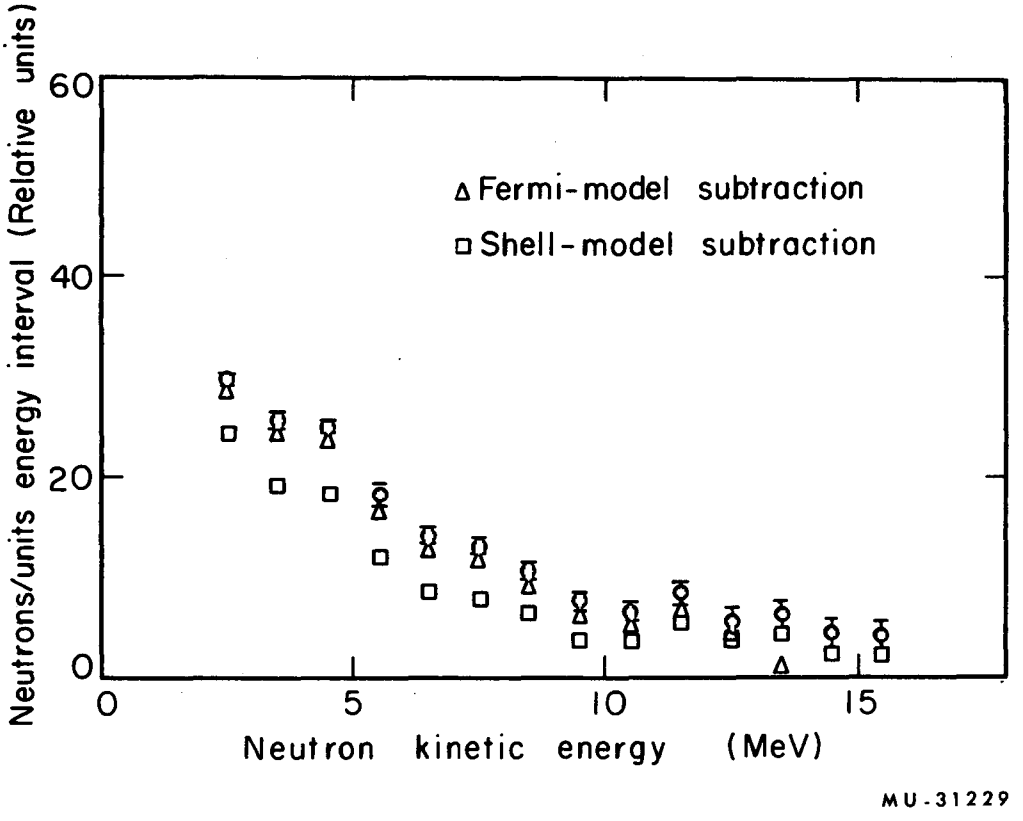

Fig. 18. Neutron-energy spectrum for calcium.

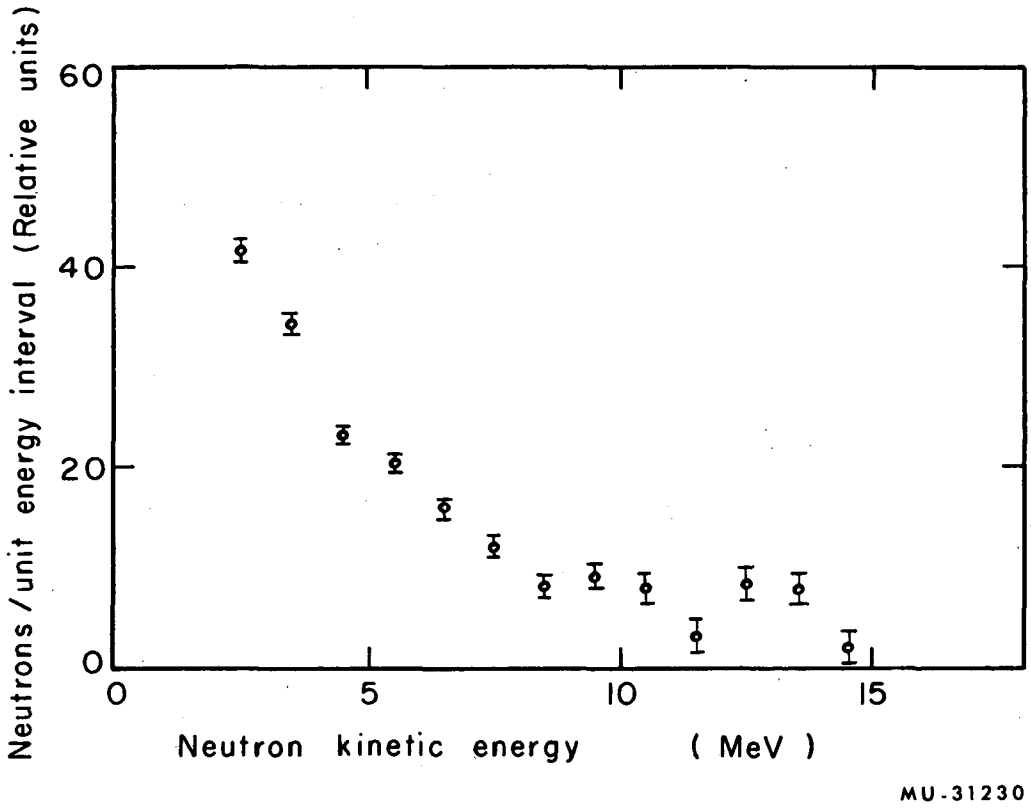

Fig. 19. Neutron-energy spectrum for iron.

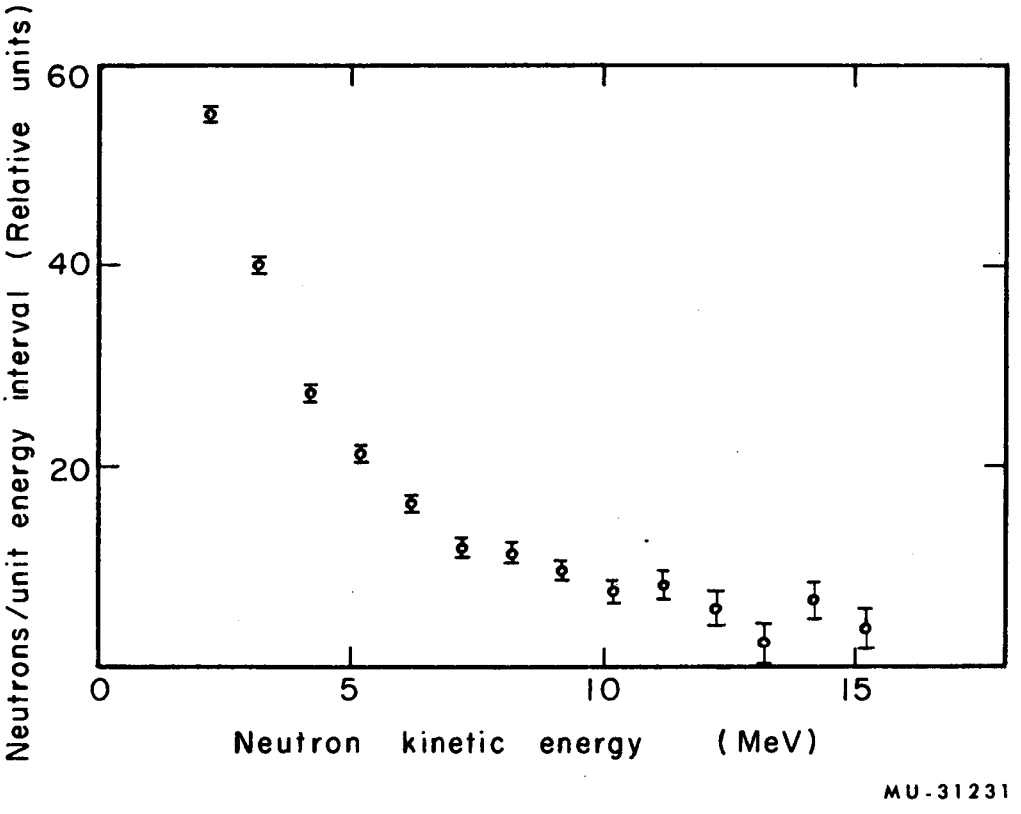

Fig. 20. Neutron-energy spectrum for silver.

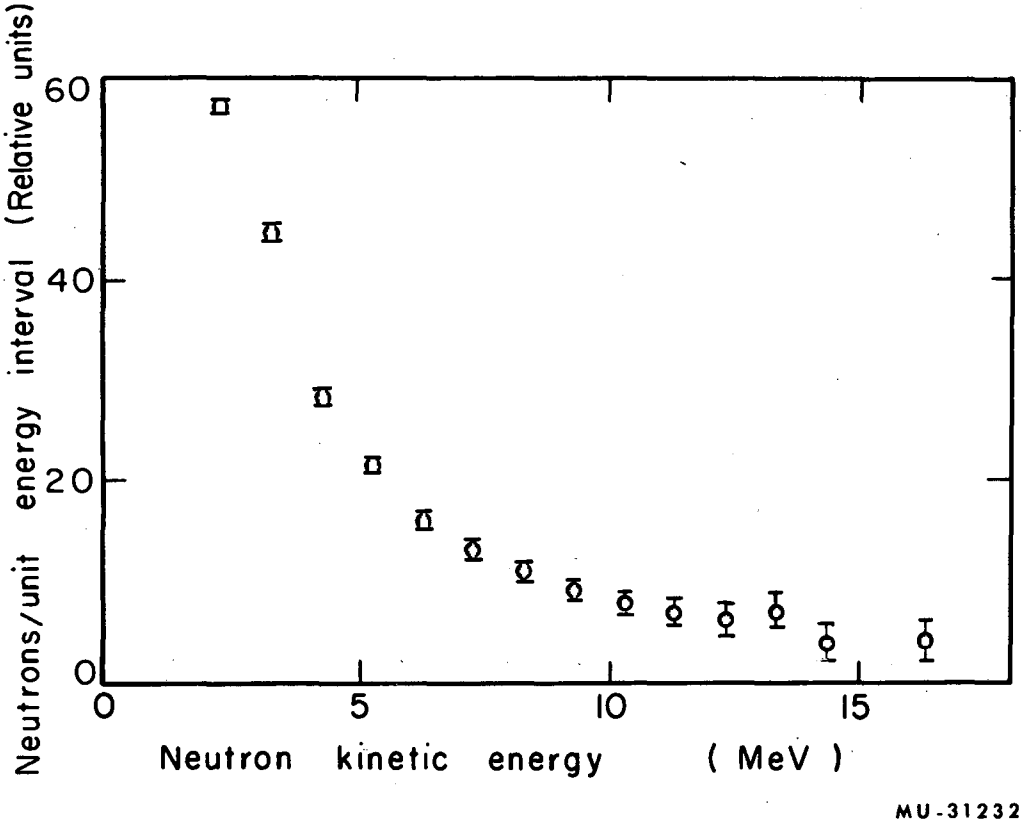

Fig. 21. Neutron-energy spectrum for iodine.

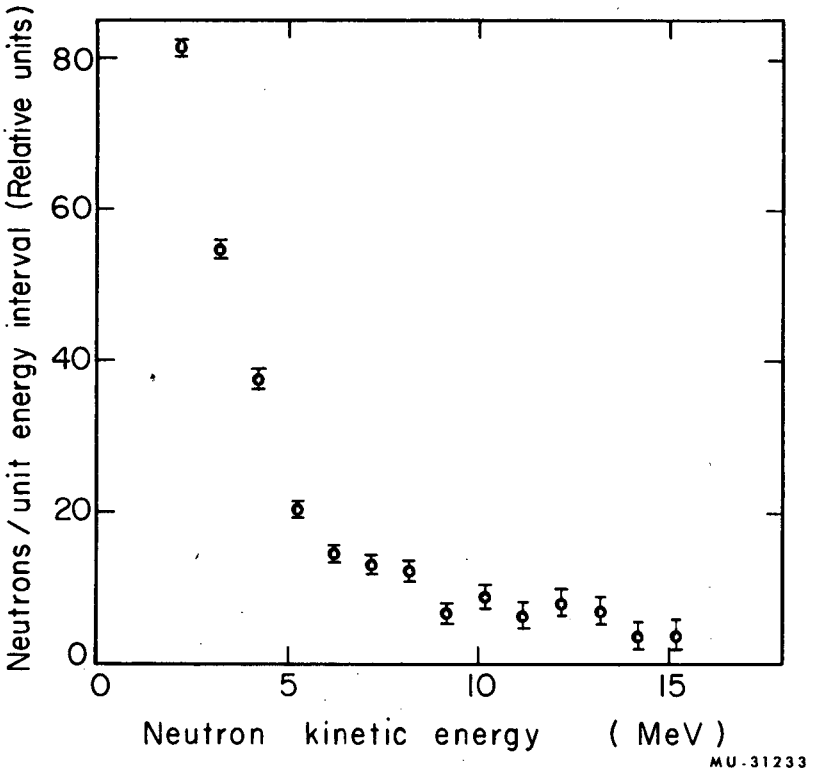

Fig. 22. Neutron-energy spectrum for gold.

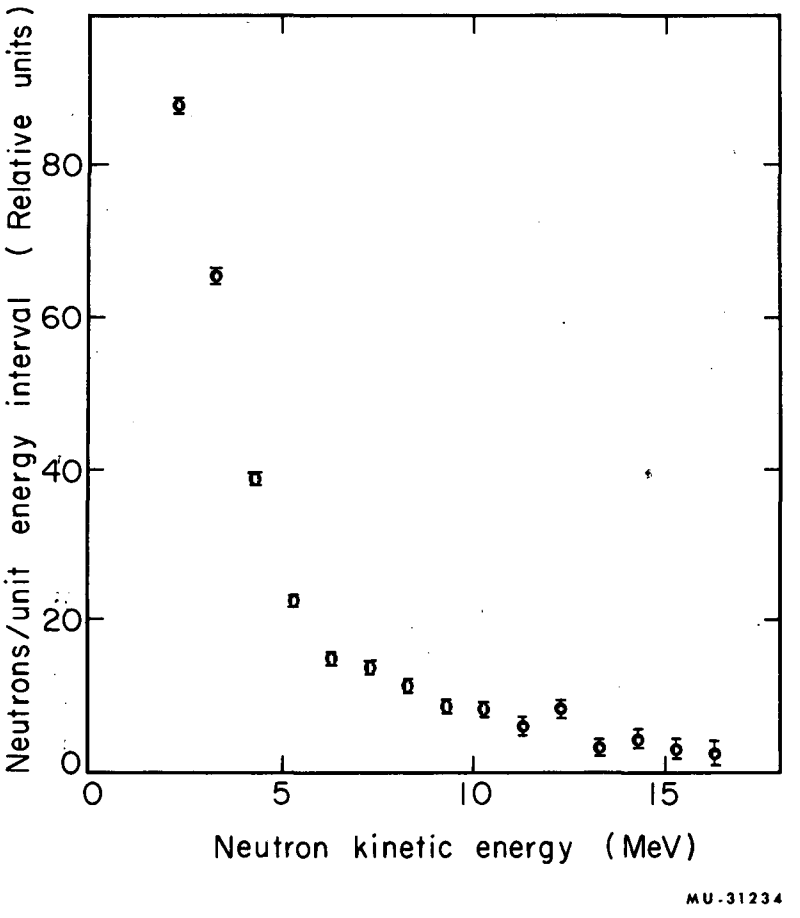

Fig. 23. Neutron-energy spectrum for lead.

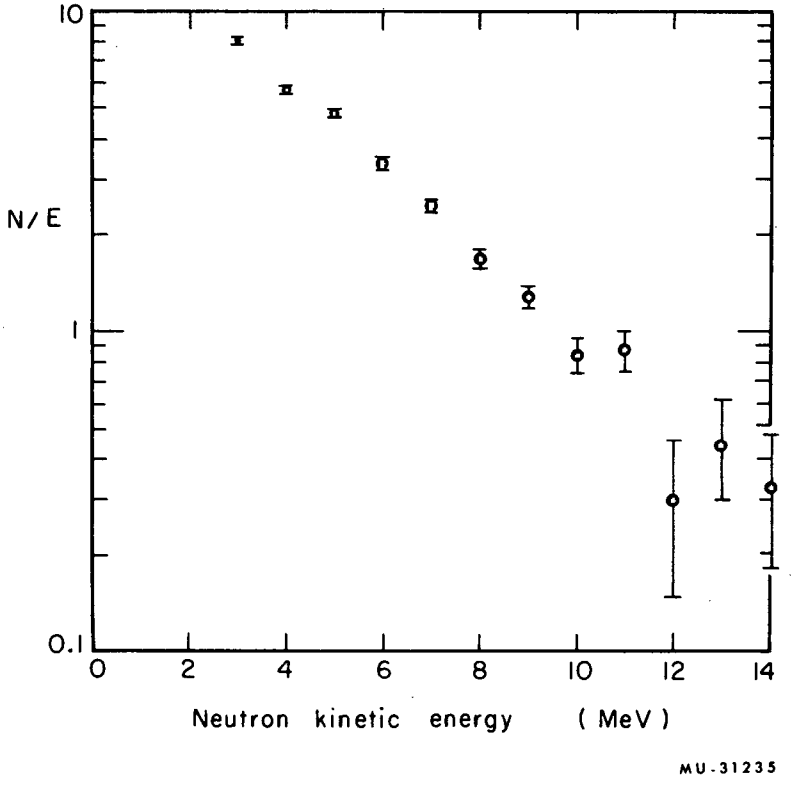

Fig. 24. Aluminum nuclear-temperature plot.

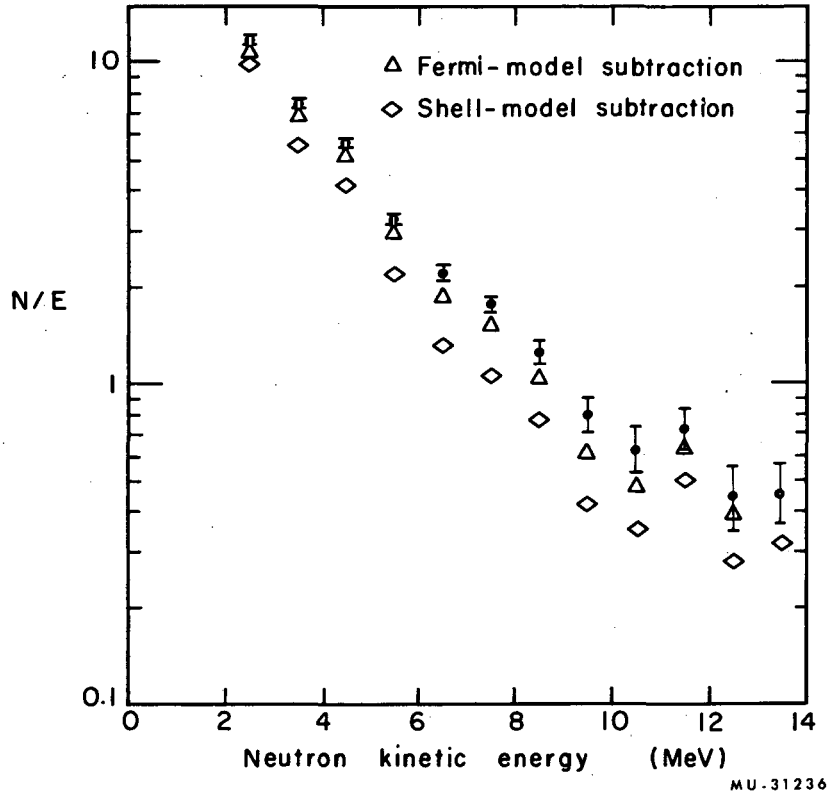

Fig. 25. Calcium nuclear-temperature plot.

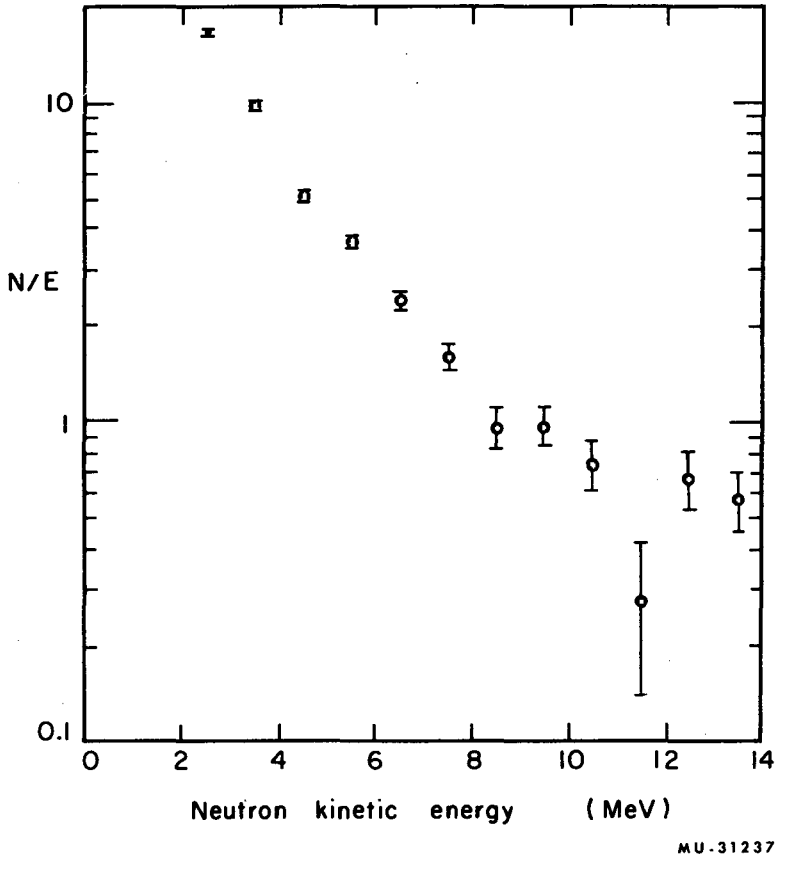

Fig. 26. Iron nuclear-temperature plot.

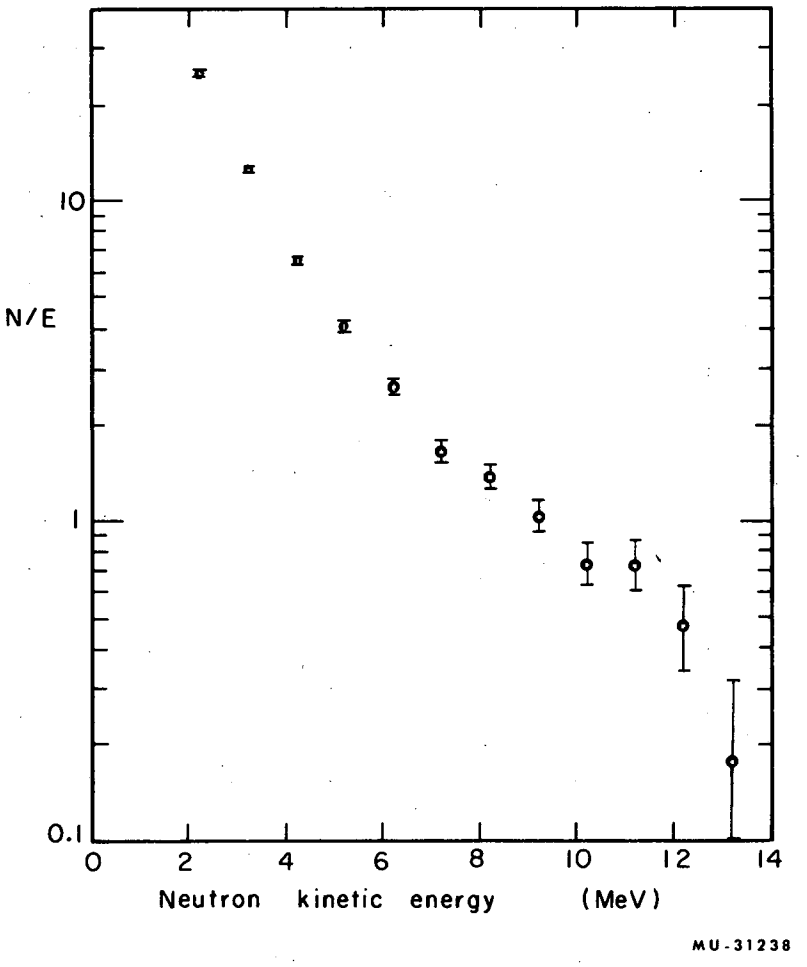

Fig. 27. Silver nuclear-temperature plot.

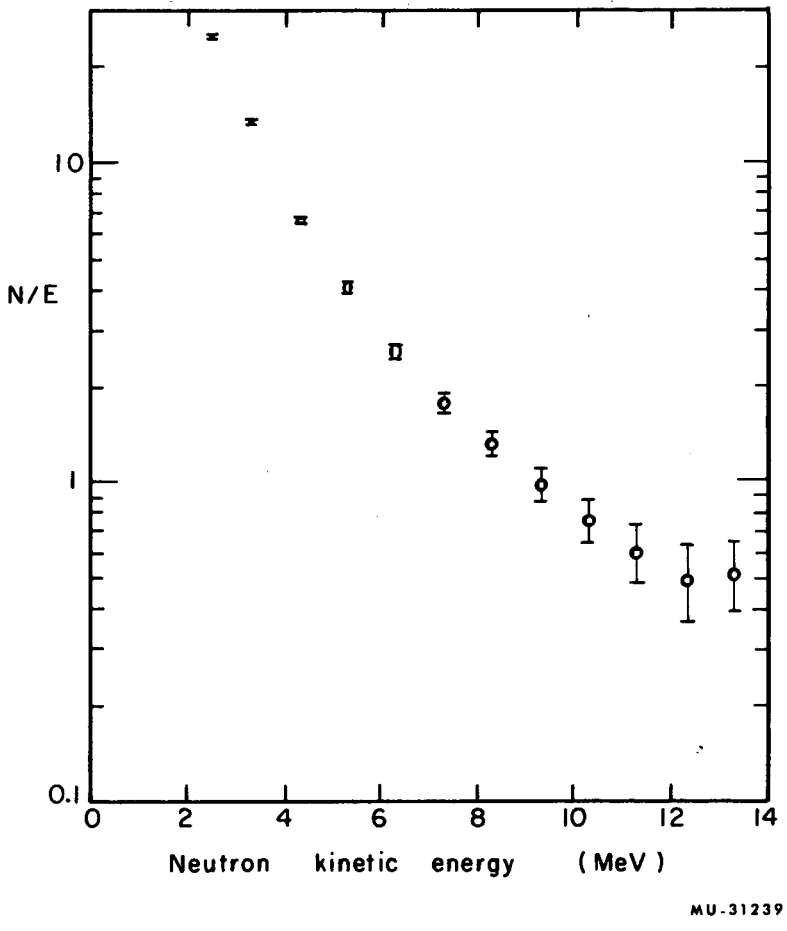

Fig. 28. Iodine nuclear-temperature plot.

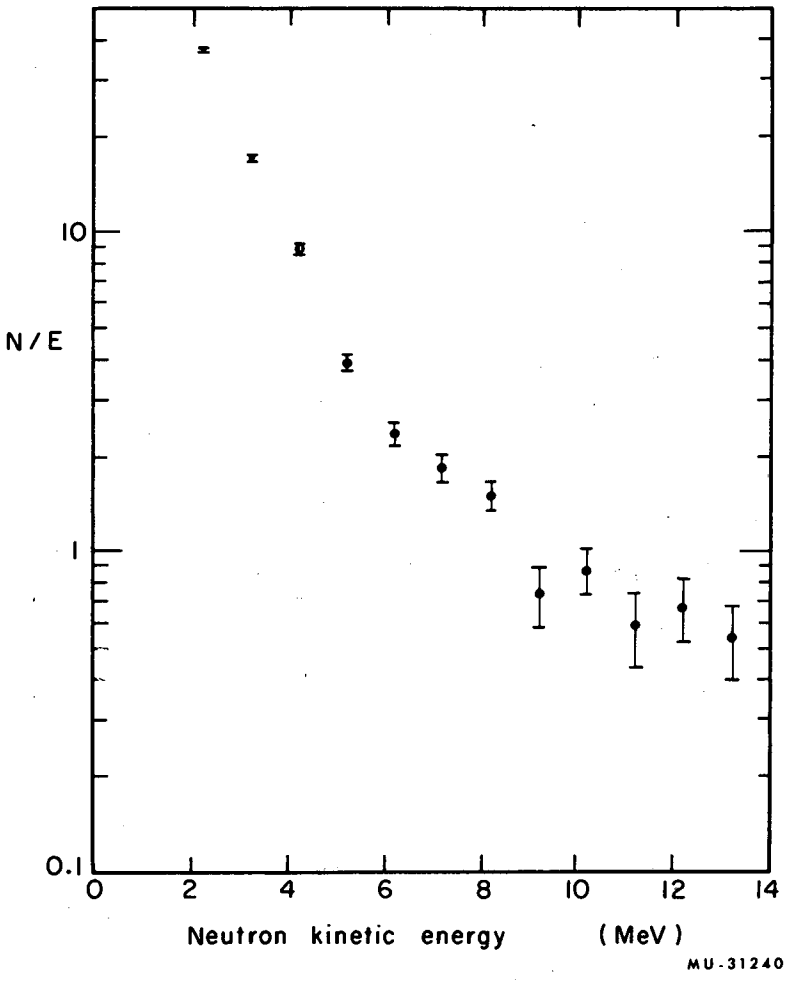

Fig. 29. Gold nuclear-temperature plot.

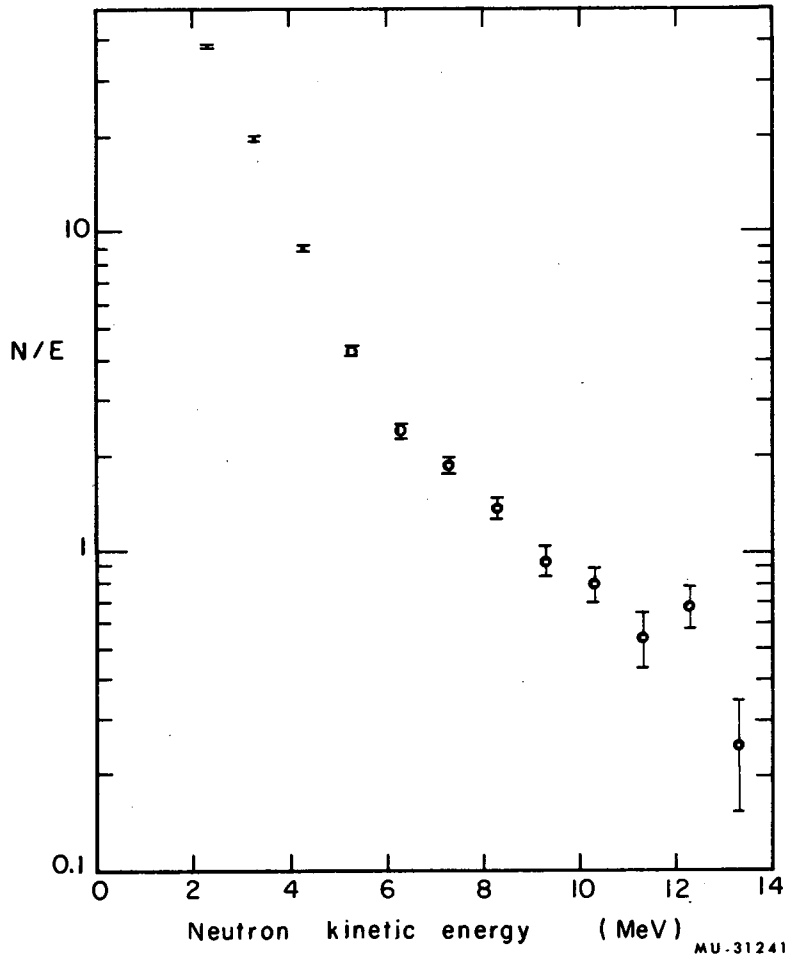

Fig. 30. Lead nuclear-temperature plot.

to observed spectra (i. e., the inverse slope). If the excitation energies are not so high that multiple neutron emission is prevalent and if the excitation-energy distributions are not extremely broad, then the "mean nuclear temperature" may still remain as a useful parameter in the interpretation of observed neutron spectra.

With the above reservations in mind, estimates of the nuclear temperatures and their errors were made from the four lowest energy data points of the nuclear-temperature plots. The energy range of these data points is from about 2 to slightly above 5 MeV. It is assumed that direct neutron emission will be relatively small and have little effect on the data points in this region. The nuclear temperatures are shown in Fig. 31 along with results from 160-MeV proton scattering, and from 14 MeV and other low-energy inelastic neutron scattering experiments.[10]

The nuclear temperatures were also calculated in accordance with evaporation theory from Eq. (9) above. The excitation energies of the compound nuclei U_0 were estimated from

$$U_0 = \bar{n}(B+2\theta) + B/2 ,$$

where $\bar{n}$ is the average neutron emission, θ is the temperature of the residual nucleus, and B is the average neutron binding energy in the compound nucleus. It is assumed the average neutron has a kinetic energy of 2θ and the average residual nucleus is left with energy B/2. The excitation energy U of the residual nucleus after emission of the first neutron is then found from

$$U = U_0 - (B+2\theta), \tag{21}$$

or from

$$U = (\bar{n} - 1)(B+2\theta) + B/2.$$

The values of the level-density parameters "a" are determined from Eq. (10). Values used for B are given in Table V. Values of θ and U are found which are simultaneously consistent with Eqs. (9) and (21). The calculated temperatures are listed under θ_c of Table V and are plotted in Fig. 31.

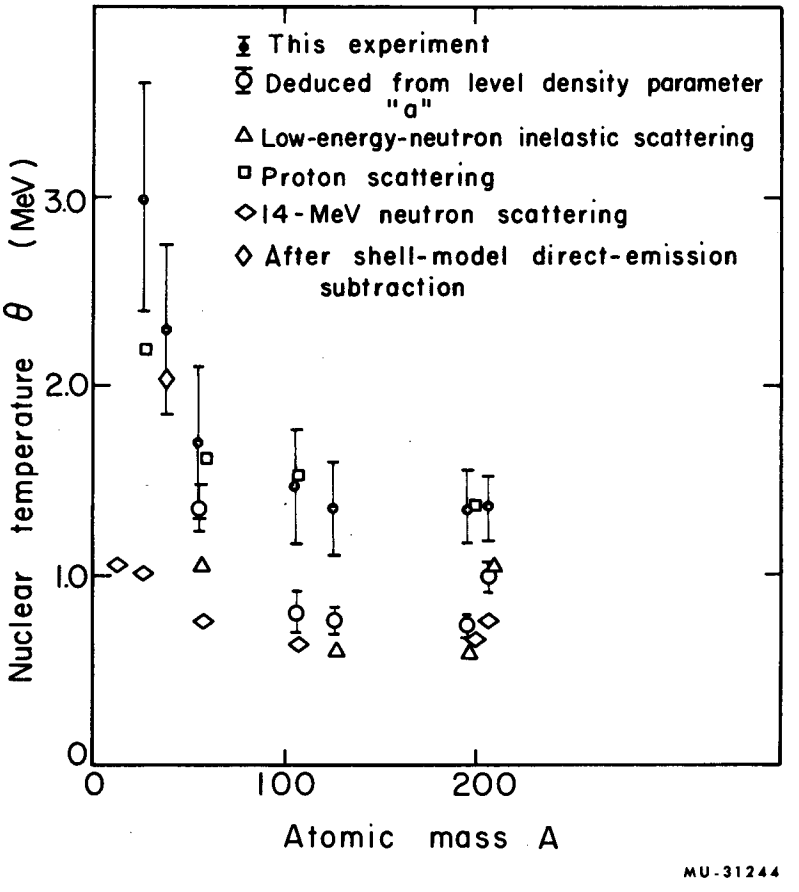

Fig. 31. Nuclear temperatures.

Table V. Summary of Results

Target nucleus	Compound nucleus	Residual nucleus	B_N	$\bar{n}$	θ	θ_c	U_0	U	a	a_c
Pb	Tl^{204}	Tl^{203}	5.24	1.64	1.35	0.99	15.6	7.7	11.9	7.7
	Tl^{206}	Tl^{205}		±0.06	±0.17	±0.08	±1.8	±1.7		±1.8
	Tl^{207}	Tl^{206}								
	Tl^{208}	Tl^{207}								
Au	Pt^{197}	Pt^{196}	5.5	1.60	1.37	0.73	16.0	7.7	19.0	7.5
				±0.06	±0.20	±0.07	±1.6	±1.6		±2.2
I	Te^{127}	Te^{126}	6.4	1.46	1.35	0.76	16.5	7.4	17.5	7.6
				±0.06	±0.25	±0.07	±1.8	±1.7		±2.2
Ag	Pd^{107}	Pd^{106}	6.3	1.52	1.47	0.80	17.2	8.0	16.8	6.9
	Pd^{109}	Pd^{108}		±0.06	±0.30	±0.11	±2.5	±2.4		±2.5
Fe	Mn^{56}	Mn^{55}	7.3	1.11	1.70	1.35	15.5	4.8	6.5	4.8
				±0.05	±0.40	±0.12	±2.1	±1.9		±1.4
Ca	K^{40}	K^{39}	7.8	0.73	2.30	—	13.0	1.3	4.0	5.1
				±0.06	±0.45	—	±2.2	±2.1		±5.0

B_N (MeV) = neutron binding energy in compound nucleus (weighted mean, where appropriate). See Ref. 35.

$\bar{n}$ = average neutron emission. See Ref. 34.

θ (MeV) = nuclear temperature measured in this experiment.

θ_c (MeV) = calculated nuclear temperature

U_0 (MeV) = compound-nucleus excitation energy.

U (MeV) = residual-nucleus excitation energy.

a $(MeV)^{-1}$ = nuclear level-density parameter from shell-model calculation. See Sec. II. A.

a_c $(MeV)^{-1}$ = nuclear level-density parameter calculated from this experiment.

Level-density parameters "a" were also calculated from Eq. (9) by using the measured nuclear temperatures and Eq. (21) to obtain the excitation energies of the residual nucleus. The results are listed in Table V. Figure 32 shows the level-density parameters found from this experiment along with those found from the shell-model calculation[19] and from low-energy inelastic neutron scattering measurements[10] (corresponding to the points on the nuclear-temperature plot).

It is seen from Fig. 31 that the nuclear temperatures measured here are in agreement with those from high-energy proton bombardment, with the exception of Al. The temperatures obtained from inelastic neutron scattering are generally much smaller.

In light elements, the level density is small and one doesn't expect the statistical model to be valid.[4] Also, the direct emission probably becomes large enough to markedly change the spectrum, resulting in too high a nuclear temperature which is not characteristic of the evaporation spectrum. After the direct-emission spectrum from the shell-model calculation was subtracted from the Ca spectrum, the temperature decreased by about 10%, as is shown in Fig. 31. All other direct-emission subtractions had a nearly negligible effect on the temperature.

For these reasons, one would expect the nuclear-temperature measurements to be more meaningful for the heavier target nuclei. However, for the four heaviest nuclei, the residual-nucleus excitation energies are comparable to neutron binding energies, which results in frequent multiple neutron emission; i.e., average neutron emissions that are considerably greater than 1.0. These features are shown in Fig. 33. Hence, it appears that the most favorable of the seven target nuclei for comparison with other measurements and compound nuclear theory is Fe. Several different measurements are listed in Table VI along with that from this experiment.

Considering the accuracy of the measurement, the temperature of Fe found from μ^--meson capture is not inconsistent with the measurements from four different means of nuclear excitation. The nuclear temperature deduced from the shell-model prediction of the level-density

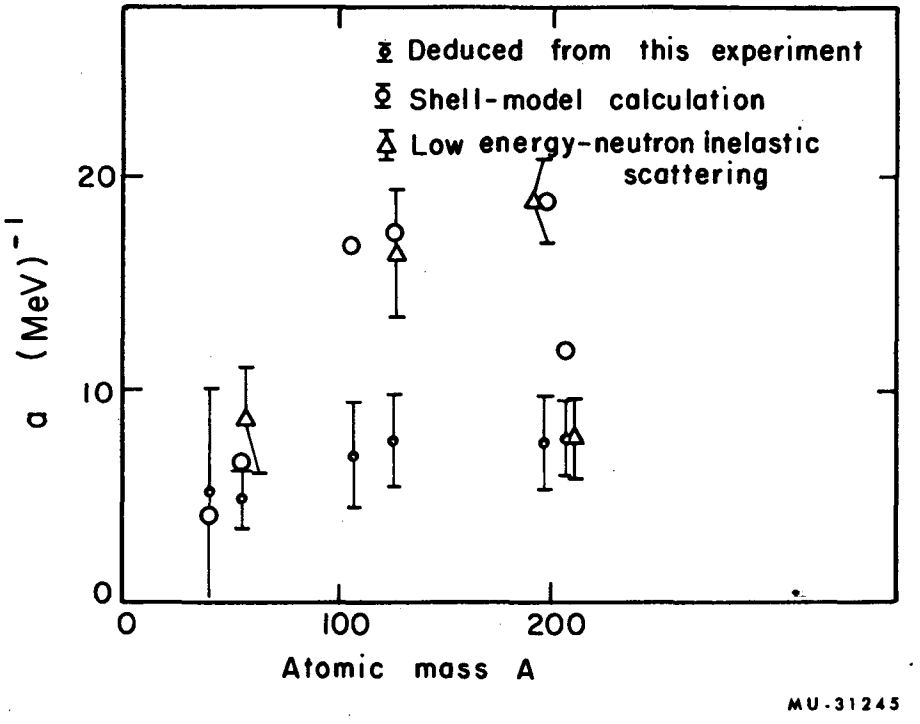

Fig. 32. Nuclear level density parameter.

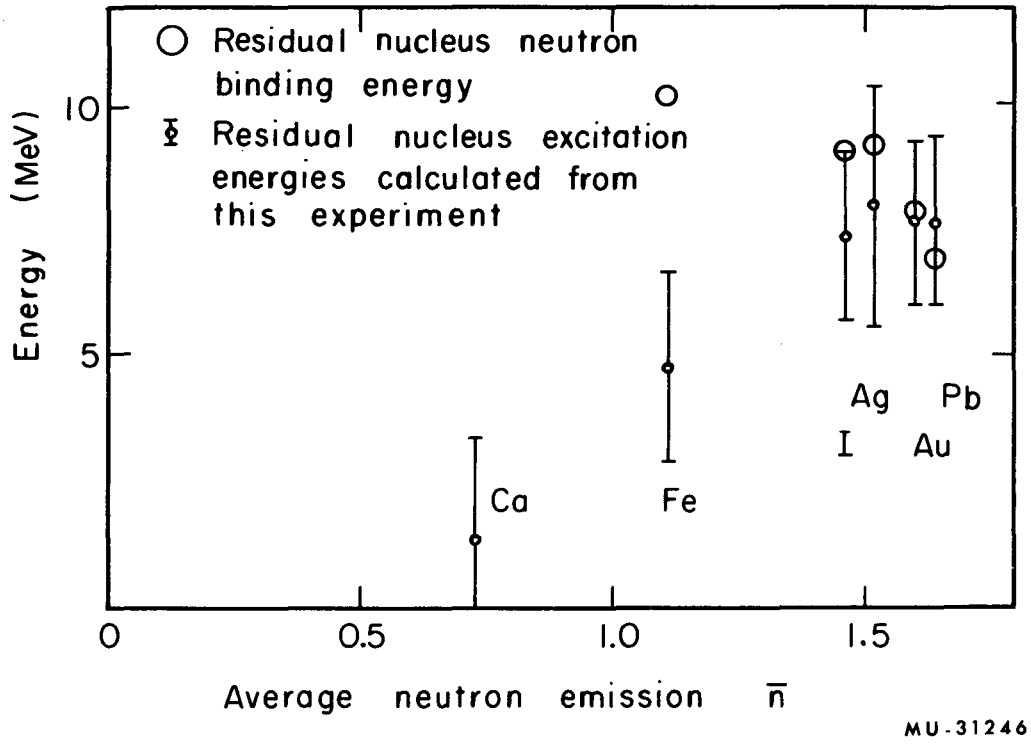

Fig. 33. Average excitation of residual nucleus after emission of the first neutron.

Table VI. Comparison of temperatures obtained from various methods of exciting Fe and other nuclei of neighboring atomic masses.

Type Data	Incident Energy (MeV)	Target Nucleus	Residual Nucleus	Residual Energy U (MeV)	Nuclear Temp (MeV)	Ref. No.
(μ^-, n)	—	Fe^{56}	Mn^{56}	4.8 ± 1.9	1.7 ± 0.4	This exp.
(n,n)	7	Fe^{56}	Fe^{56}	5.0	0.95	6
(n,n)	14	Fe	Fe	—	0.76 ± 0.08	5
(p,p')	10	Fe	natural	5.0	1.05	8
(p,α)	17	Co^{59}	Fe^{56}	7.0	1.46	9

parameter "a" is consistent with the experimental value. Furthermore, the level-density parameter "a" deduced from the temperature measurement is consistent with measured and theoretical values.

Multiple neutron emission probably has the effect of giving relatively more high-energy neutrons to an energy spectrum. This, combined with the lack of low-energy data points near the evaporation peak, results in a temperature measurement considerably higher than the true mean value. This consideration is born out by the high temperatures found for the heaviest nuclei from this experiment and from the high-energy proton experiment, as compared to low-energy neutron experiments where the excitation energies were lower. The disagreement is less for Pb where shell effects result in a predicted low value for "a" and in a higher nuclear temperature for a given excitation energy.[19]

One of the unresolved problems in the interpretation of experimental observations by statistical theory is the dependence of nuclear temperature upon excitation energy.[10] In principle, the temperature should be independent of the compound-nucleus excitation energy U_0 if the residual-nucleus excitation energy U is held fixed. In practice, it is found that the temperature increases with U_0 for fixed U. Although it is believed that in this experiment the disagreements in nuclear temperatures stem from multiple-emission effects, it is also possible that an anomalous temperature-energy dependence is partly responsible.

The method of exciting a nucleus by μ^--meson capture is quite different than any other. Energy is supplied to the nucleus, while little momentum is imparted as compared to a scattering process. Also, the energy is supplied to the nuclear matter uniformly since the μ^--meson is weakly interacting and therefore does not interact preferably near the surface. The process of neutron emission from the nuclear capture of μ^- mesons should be more amenable to accurate model predictions of excitation-energy functions than is scattering. By measuring the average neutron emission one can determine the extent to which the simple evaporation theory is valid. If one would

choose a target to provide a combination of compound and residual nuclei with high binding energies, multiple neutron emission could perhaps be minimized or eliminated, thereby making the experimental interpretation in terms of compound nuclear theory more valid and useful.

ACKNOWLEDGMENTS

I am grateful to Professor Burton J. Moyer for several discussions and for helpful advice relative to this experiment and, more importantly, for the rewarding experience of associating for several years with a man who is an inspiring teacher, both in the classroom and laboratory, and who possesses a great warmth and personal concern for the individual student.

I am grateful to Drs. Selig Kaplan, Robert Pyle, Jagdish Baijal, and Justo Diaz for their efforts in the preparation and operation of the experiment, and to Drs. Kaplan and Pyle for useful discussions during the data analysis and interpretation.

APPENDICES

A. Neutron-Escape Probability

A neutron with energy E created at point y has a probability of traversing a distance x to the nuclear surface of

$$P(y, E) = \exp[-x/\lambda(E)],$$

where $\lambda(E)$ is the mean free path in nuclear matter (Appendix B). The kinematical terms used here are defined in Sketch A1.

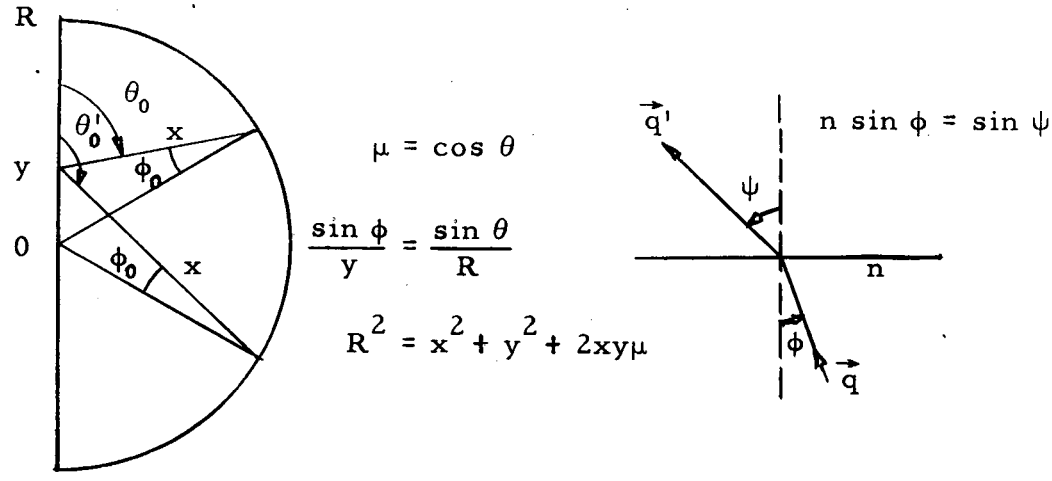

Sketch A1.

The neutron has a probability $T(y, \phi)$ of passing through the surface if $\phi < \phi_0$, where

$$n \sin\phi_0 = 1 \text{ and } n = q/q'.$$

The momenta inside and outside the nucleus are q and q', respectively. The transmission coefficient is given by

$$T(y, \phi) = \frac{4\, q \cos\phi\, q' \cos\psi}{(q \cos\phi + q' \cos\psi)^2},$$

which becomes

$$T(y, \mu) = \frac{4\, f(y, \mu)/n}{[1 + f(y, \mu)/n]^2},$$

where

$$f(y, \mu) = \cos\psi/\cos\phi$$

$$= \left[\frac{1 - n^2(y/R)^2(1 - \mu^2)}{1 - (y/R)^2 (1 - \mu^2)} \right]^{1/2}$$

Also,

$$x(y, \mu) = - \mu y + [(R^2 - y^2) + \mu^2 y^2]^{1/2}.$$

After an integration over the volume of the sphere with the restriction on the solid angle Ω' that $\phi < \phi_0$ and normalizing, the escape probability becomes

$$P(E) = \frac{3}{2R^3} \int_0^R \left\{ \int_{\Omega'} T(y,\mu)\, p(y, E)\, d\mu \right\} y^2 dy.$$

The double integral was evaluated numerically and the results for various values of R are shown in Fig. 34.

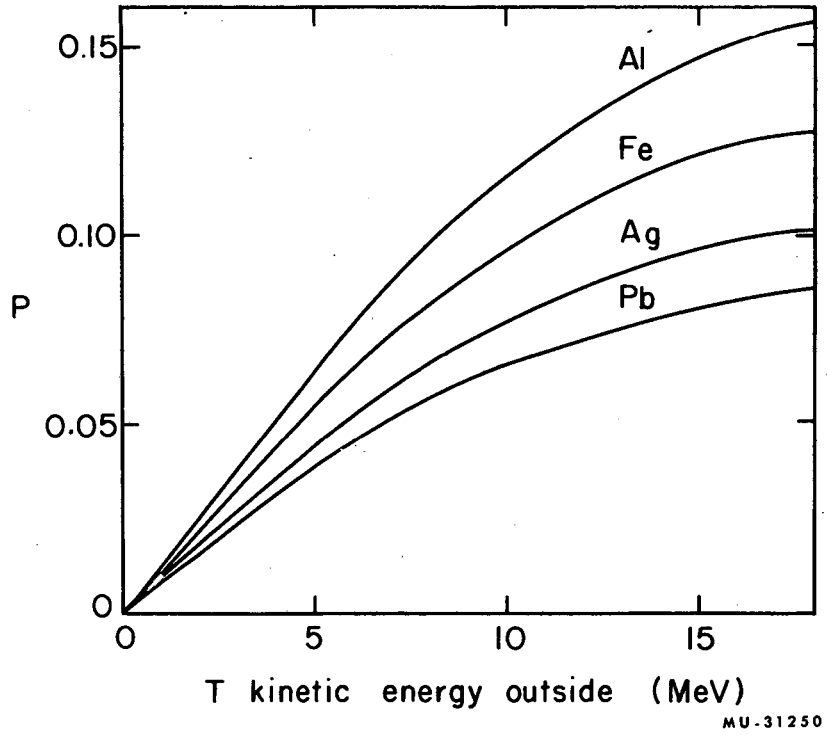

Fig. 34. Neutron-escape probability from nuclei; r_0 = 1.25 fermi.

B. Nuclear Mean Free Path

The mean free path in nuclear matter was determined from the theory of the optical model. The expression is

$$\lambda = 1/2K_I,$$

where

$$K = K_R + i\,K_I.$$

The momentum inside the nucleus is K, and outside the nucleus it is k. We have

$$K^2 = k^2 - 2M(V + i\,W),$$

where V and W are the real and imaginary parts of the optical potential (see Sketch B1).

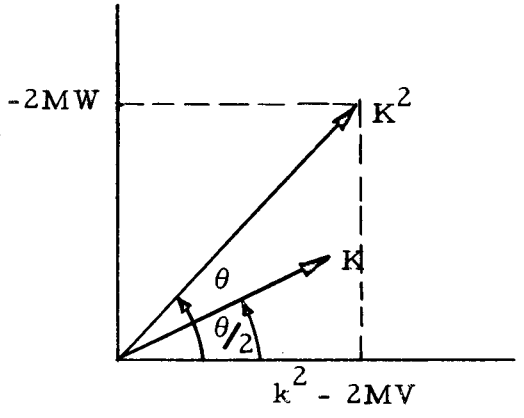

Sketch B1.

Solving for the mean free path, one obtains

$$\lambda(k) = \frac{1}{2K \sin\theta/2},$$

where

$$\sin\theta/2 = \left[\frac{1 - 1/(1+x^2)^{1/2}}{2}\right]^{1/2}$$

and

$$x = \frac{-2MW(k)}{k^2 - 2MV(k)}.$$

The potentials[45] used are

$$V(k) = -53 + 0.6\ (k^2/2M)$$

and

$$W(k) = -2.6 - 0.4\ (k^2/2M).$$

The results are shown in Fig. 35.

C. Efficiency Function

Assuming single collisions only, the probability of a neutron interacting with a proton in a scintillator of thickness x is

$$F(E) = 1 - \exp[-nx\sigma(E)],$$

where $\sigma(E)$ is the total n-p cross section. An analytic fit to the cross section[46] was determined to be (see Fig. 36)

$$\sigma(E) = (4.85/E^{1/2}) - 0.58 \text{ barns}.$$

The hydrogen density is[47]

$$n = 0.483 \times 10^{23}/\text{cc}.$$

The scintillator thickness is

$$x = 2.53 \text{ cm}.$$

With these values, the efficiency function becomes

$$F(E) = 1 - 1.074\ \exp(-0.592/E^{1/2}).$$

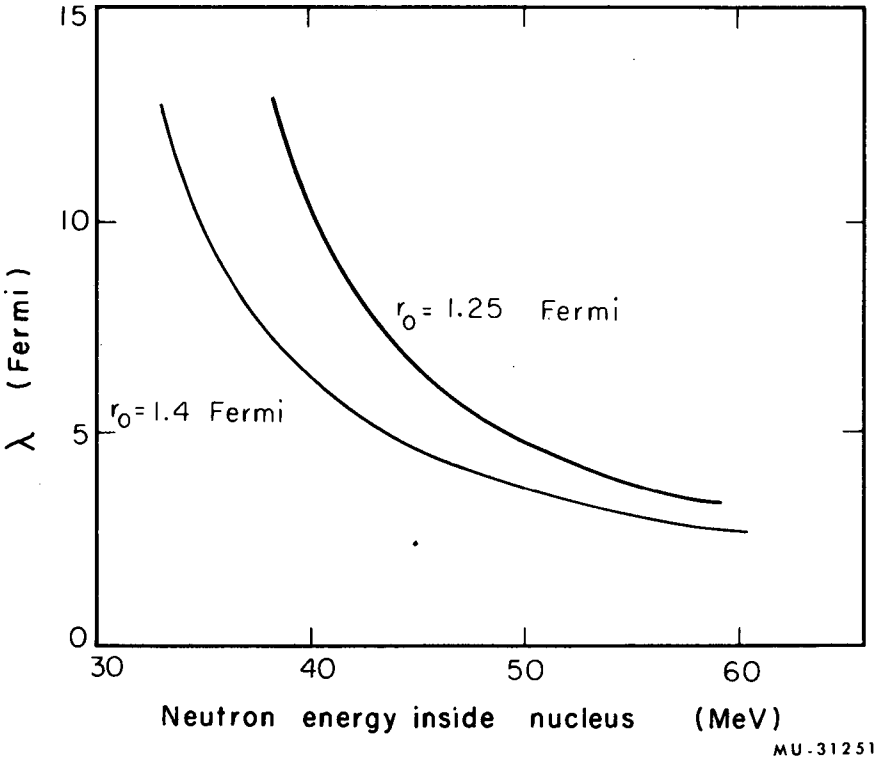

Fig. 35. Nuclear mean free path.

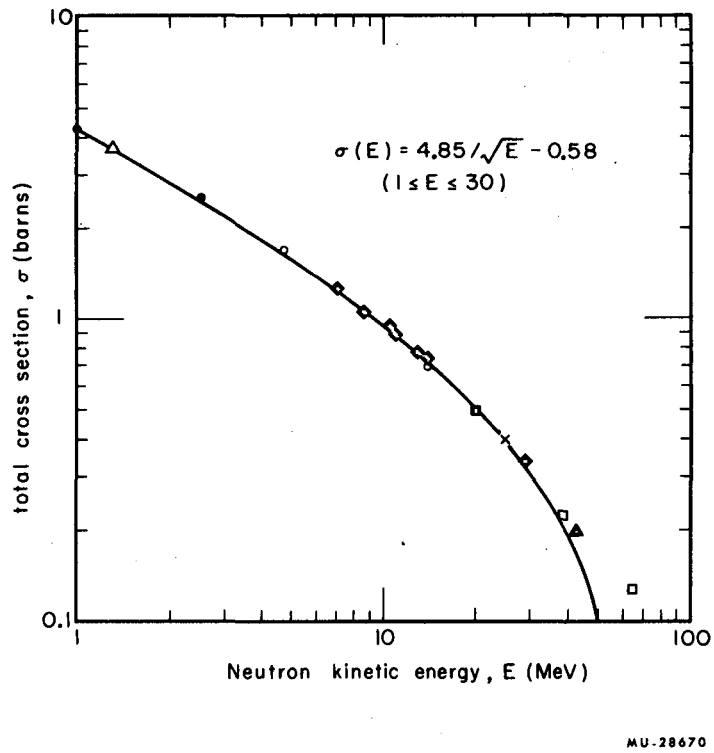

Fig. 36. Total neutron-proton cross section (ref. 46).

REFERENCES

1. M. Conversi, E. Pancini, and O. Piccioni, Phys. Rev. 71, 209 (1947).
2. S. N. Kaplan, B. J. Moyer, and R. V. Pyle, Phys. Rev. 112, 968 (1958).
3. H. Morinaga and W. F. Fry, Nuovo Cimento, Ser. IX, 10, 308 (1953).
4. K. J. LeCouteur, Nuclear Reactions I (1959), Chapt. VII.
5. E. R. Graves and L. Rosen, Phys. Rev. 89, 343 (1953).
6. D. B. Thomson, Doctoral thesis, University of Kansas (1960).
7. E. E. Gross, The Absolute Yield of Low-Energy Neutrons from 190-MeV Proton Bombardment of Gold, Silver, Nickel, Aluminum, and Carbon (thesis) UCRL-3330, February, 1956 (unpublished).
8. N. Hintz and V. Meyer, University of Minnesota Linear Accelerator Laboratory Progress Report 59, 1961.
9. R. Sherr and F. P. Brady, Phys. Rev. 124, 1928 (1961).
10. David Bodansky, Ann. Rev. Nucl. Sci. 12, 79 (1962).
11. J. Steinberger and H. B. Wolfe, Phys. Rev. 100, 1490 (1955); O. Piccioni, Phys. Rev. 74, 1754 (1948).
12. J. Tiomno and J. A. Wheeler, Rev. Mod. Phys. 21, 153 (1949).
13. J. M. B. Lang, Proc. Phys. Soc. (London) A65, 995 (1952).
14. F. T. Cole, (thesis), Cornell University, 1953 (unpublished).
15. P. Singer, Nuovo Cimento (10), 23, 477 (1962).
16. P. Singer, Phys. Rev. 124, 1602 (1961).
17. Selig Kaplan, B. Macdonald, Burton J. Moyer, Robert V. Pyle, and Justo Diaz, Nuclear Excitation Induced by a μ^- Meson Capture, UCRL-8795 Rev. (abstract), June, 1959.
18. V. Weisskopf, Phys. Rev. 52, 295 (1937).
19. D. W. Lang, Nuclear Phys. 26, 434 (1961).
20. T. D. Newton, Can. J. Phys. 34, 804 (1956).
21. R. Huby, Phil. Mag. 40, 685 (1949).
22. D. West, Rep. Prog. Phys. 21, 271 (1958).
23. E. Fermi and E. Teller, Phys. Rev. 72, 399 (1947).

24. R. M. Tennent, Prog. Elem. Particle Cosmic Ray Phys. 5, 367 (1960).
25. H. K. Ticho, Phys. Rev. 74, 1337 (1948); J. W. Keuffel, F. B. Harrison, T. N. K. Godfrey, and G. T. Reynolds, Phys. Rev. 87, 942 (1952); A. Alberigi-Quaranta and E. Pancini, Nuovo Cimento 11, 607 (1954).
26. J. A. Wheeler, Rev. Mod. Phys. 21, 133 (1949).
27. W. F. Fry, Phys. Rev. 90, 999 (1953).
28. K. W. Ford and J. G. Willis, Calculated Properties of μ^- Mesonic Atoms, Los Alamos Scientific Laboratory Report LAMS 2387, November 1959.
29. H. Primakoff, Rev. Mod. Phys. 31, 802 (1959).
30. K. J. LeCouteur and D. W. Lang, Nucl. Phys. 13, 32 (1959).
31. L. Wilats, Phys. Rev. 101, 1805 (1956).
32. E. I. Dolinsky and L. D. Blokhintsev, Nucl. Phys. 10, 527 (1959).
33. Elihu Lubkin, Ann. Phys. 11, 414 (1960).
34. Burns Macdonald (Lawrence Radiation Laboratory), private communication.
35. Handbook of Chemistry and Physics (Chemical Rubber Publishing Co., Cleveland, Ohio 1962).
36. F. Everling, L. A. König, J. H. E. Mattauchaud, and A. H. Wapstra, Nucl. Phys. 18, 529 (1960).
37. R. Batchelor, W. B. Gilboy, J. B. Parker, and J. H. Towle, Nucl. Instr. and Methods 13, 70 (1961).
38. F. D. Brooks, Nucl. Instr. and Methods 4, 151 (1959).
39. R. B. Owen, Nucleonics 17, 9, 92 (1959).
40. Leona Stewart, Phys. Rev. 98, 740 (1955).
41. Wilmot N. Hess, Neutrons from (α, n) Sources, Lawrence Radiation Laboratory Report UCRL-3839, July 1957 (unpublished).
42. B. E. Watt, Phys. Rev. 87, 1037 (1952).
43. Peter Cziffra and Michael J. Moravcsik, A Practical Guide to the Method of Least Squares, UCRL-8523 Rev., June 1959 (unpublished).

44. W. O. Lock, High Energy Nuclear Physics, 110 (1960).

45. F. Bjorklund and S. Fernbach, Exact Phase-Shift Calculation for Nucleon Nuclear Scatter, UCRL-5028, September 1958 (unpublished).

46. D. J. Hughes, B. A. Magurno, and M. K. Brussel, Neutron Cross Sections, Brookhaven National Laboratory, 74 (1960).

47. W. B. Reid (Nuclear Enterprises Ltd., Winnepeg, Canada), August 13, 1962 (private communication).